RETRIEVALS OF AEROSOL SINGLE SCATTERING ALBEDO BY MULTIWAVELENGTH LIDAR MEASUREMENTS: EVALUATIONS WITH NASA LANGLEY HSRL-2 DURING DISCOVER-AQ FIELD CAMPAIGNS.

Daniel Pérez-Ramírez[1,2], David N. Whiteman[3,4], Igor Veselovskii[5], Peter Colarco[6], Mikhail Korenski[5], and Arlindo da Silva[7]

[1]Applied Physics Department, University of Granada, 18071, Granada, Spain

[2]Andalusian Institute for Earth System Research (IISTA-CEAMA), 18006, Granada, Spain

[3]Mesoscale Atmospheric Processes Laboratory, NASA Goddard Space Flight Center, 20771, Greenbelt, Maryland, United States.

[4]Howard University Beltsville Campus, 20705, Beltsville, Maryland, United States,

[5]Physics Instrumentation Center of General Physics Institute, Troitsk, Moscow, Russia

[6]Atmospheric Chemistry and Dynamics Laboratory, NASA Goddard Space Flight Center, 20771, Greenbelt, Maryland, United States.

[7]Global Modeling and Assimilation Office, NASA Goddard Space Flight Center, 20771, Greenbelt, Maryland, United States.

Correspondence to: Daniel Perez-Ramirez; E-mail: dperez@ugr.es;

ABSTRACT

This work focuses on the study and evaluation of the retrievals of aerosol complex refractive index ($m = m_r + im_i$) and single scattering albedo (SSA) from the inversion of multi-wavelength lidar measurements, particularly of three backscattering coefficients (β) at 355, 532 and 1064 nm and two extinction coefficients (α) at 355 and 532 nm, typically known as the stand-alone 3β+2α lidar inversion. The focus is on the well-known regularization technique for spherical particles. It is well known that constraints in the range of refractive indices allowed in the inversion are essential, both for the real (m_r) and imaginary (m_i) parts, due to the under-determined nature of the problem. Usually these constraints are fixed for a given set of inversions. Using a large database of AERONET retrievals, correlations between retrieved m_r and m_i are observed and those correlations together with results from the GOCART model are used to define optimized, case-dependent, constraints in the stand-alone 3β+2α lidar inversion. For each inversion performed, the optimized constraints are computed from the 3β+2α data using a-priori information of extinction-to-backscattered ratio (LR) and the Angstrom exponent computed with α at 355 and 532 nm. The stand-alone 3β+2α lidar inversion with optimized, case-dependent, constraints is applied to airborne NASA LaRC HSRL-2 experimental measurements during DISCOVER-AQ. The optimized constraints selected from the measured 3β+2α are compared with the typing classification based on additional multiwavelength depolarization measurements, showing consistency between aerosol size and absorption range and aerosol typing. Evaluations of the SSA retrieved by the stand-alone 3β+2α lidar inversion with optimized constraints are done by comparisons with correlative airborne in-situ measured SSA. The agreement between both methodologies is satisfactory for most aerosol types as differences are within the uncertainties of each methodology.

1.- Introduction

Atmospheric aerosols affect the Earth-Atmosphere radiative system directly by scattering and absorbing solar radiation, and indirectly by altering the lifetime and development of clouds. In spite of the large advances in aerosol characterization and their effects, uncertainties still remain in to the effect of aerosols on global change during the coming century (Boucher et al., 2013). Actually, the latest IPCC model-based aerosol radiative forcing (ARF) estimates state that radiative forcing due to aerosol–radiation interactions is approximately -0.35 ± 0.5 W/m^2. However, although aerosol optical depth (AOD) and aerosol size are relatively well constrained in ARF calculations, uncertainties in the aerosol absorption properties (McComiskey et al., 2008; Loeb and Su, 2010) – particularly on their vertical profile (e.g. Zarzycki and Bond, 2010) - contribute significantly to the overall uncertainty in ARF. These imply a factor of two to four uncertainty in ARF computations when aerosol absorption is included in large-scale numerical models (Stier et al., 2013).

Absorbing aerosols are also important in climate feedback processes because they modify atmospheric stability in the boundary layer and free troposphere (e.g. Wendisch et al., 2008; Babu et al., 2011) and modify cloud properties (e.g.Yoshimori and Broccoli, 2008; Allen and Sherwood, 2010; Koch and Del Genio, 2010; Persad et al., 2012): Together the changes in atmospheric stability and reduction in surface fluxes affect significantly the fraction of surface-forced clouds and precipitation rates (Feingold et al., 2005; Sakaeda et al., 2011). Cloud cover is expected to decrease if absorbing aerosols are embedded in the cloud layer (e.g. Koren et al., 2004). Absorbing aerosols embedded in cloud drops enhance their absorption, which can affect the dissipation of clouds (Stier et al., 2007; Ghan et al., 2012). Therefore, improved quantification of aerosol absorption is also a current challenge for a better understanding of the role of aerosols in cloud formation and development.

Aerosol absorption can be measured by in-situ instrumentation but such instruments do not provide information about the aerosol vertical structure in the atmosphere unless they are operated on an aircraft performing vertical profiling flight patterns (e.g. Andrews et al., 2004). Ground based passive remote sensing, as for example those made within the AERONET network (Holben et al., 1998), do provide aerosol single scattering albedo (SSA) by inverting sky radiances and direct solar irradiances (Dubovik and King, 2000; Dubovik et al., 2006). However, these retrievals of SSA are only possible under certain situations – e.g. large scattering angles and aerosol loads (Holben et al., 2006) – and only provide column-integrated values. Other ground-based networks such as EARLINET/ACTRIS (Pappalardo et al., 2014) and MPLNET (Welton et al., 2002) are providing large amounts of lidar data for studying vertical structure of aerosols, but the retrieval of aerosol microphysics from lidar requires measurements at several wavelengths and current limitations in MPLNET and in EARLINET/ACTRIS instruments do not allow the same capabilities for aerosol microphysical properties vertical profiles characterization (e.g. Müller et al., 2016). For global coverage, a new generation of passive remote sensors is able to provide column-integrated SSA. Instruments such as the Ozone Monitoring Instrument (OMI - Torres et al., 2007) or the POLDER/PARASOL polarimeter (Tanré et al., 2011) are current examples. Other space sensors such as CALIPSO (Winker et al., 2010) implement lidar measurements that are providing near global coverage of vertically-resolved aerosol optical properties. CALIPSO measurements were complimented by the CATS system (Yorks et al., 2016) and will be extended by the future EarthCARE mission (Illingworth et al., 2015). However, all these space lidar systems fail in providing aerosol absorption vertical profiles.

The retrieval of aerosol absorption from remote sensing measurements usually requires solving an ill-posed inverse problem. For sun-photometry and space-polarimetry the number of available measurements is quite large providing more information in the inverse solution of aerosol size distribution and refractive index. (e.g. Dubovik and King 2000; Dubovik et al., 2006, 2011). However, for multiwavelength lidar measurements of three backscattering (β) at 355, 532 and 1064 nm and two extinction (α) coefficients at 355 and 532 nm – typically known as the stand-alone 3β+2α lidar inversion- the number of input data is only five so the problem is more under-determined than in the case of passive remote sensing (e.g. Veselovskii et al., 2005; Burton et al., 2016). Several techniques are used for inverting 3β+2α lidar data such as regularization (Müller et al., 1999a,b; Veselovskii et al., 2002; Böckman et al., 2005) and Linear Estimation (Veselovskii et al., 2012). Numerous works have been done using these retrievals (hereafter denoted as stand-alone 3β+2α lidar inversion), but focusing on particle size distribution (PSD) and their associated bulk parameters such as effective radius (r_{eff}) and particle number (N), surface (S), and volume (V) concentrations. Some examples are for biomass-burning (Alados-Arboledas et al., 2011; Müller et al., 2005, 2011;Veselovskii et al., 2015), pollution (e.g. Noh et al., 2009; Wandinger et al., 2002; Veselovskii et al., 2013), arctic haze (Müller et al., 2004) or volcanic aerosol (Navas-Guzman et al., 2013).

However, retrievals of aerosol refractive index and SSA by the stand-alone 3β+2α lidar inversion are not as successful as retrievals of bulk parameters or PSD. The real part of the refractive index (m_r) can be retrieved with uncertainties of ±0.05 (Müller et al., 1999a,b; Veselovskii et al., 2002), but only for aerosol cases where the fine mode predominates (Whiteman et al., 2018). The imaginary part (m_i), which is critical for the computation of SSA, has errors of 100% and even larger depending on the aerosol type (e.g. Veselovskii et al., 2002).

Preliminary studies (Veselovskii et al., 2005) demonstrated that m_i needs to be constrained for accurate retrievals of refractive index. Many works limit the maximum value of m_i allowed in the inversion to <= 0.01, which is not appropriate for the retrieval of aerosols when the absorption is high (e.g. Dubovik et al., 2002). Other authors suggest no constraints in m_i, but this results in very high uncertainties in the retrieval of SSA of up to 0.1 (e.g. Baars et al., 2011). To solve all these limitations in the retrieval of aerosol refractive indices by lidar measurements other approaches are being developed such as multistatic lidars (e.g. Alexandrov and Mischenko, 2016; Mischenko et al., 2016).

The objective of this work is to study and develop optimized, case-dependent constraints for the stand-alone $3\beta+2\alpha$ lidar inversion to retrieve aerosol refractive index and SSA focusing on spherical particles. The large AERONET database of aerosol microphysical properties and the Goddard Chemistry, Aerosol, Radiation, and Transport (GOCART) model are used to determine the optimized constraints. We propose a methodology to compute the optimized constraints for each inversion using measured $3\beta+2\alpha$ and *a prioiri* assumptions about the relationships between the extinction-to-backscatter ratio, otherwise known as lidar ratio (LR), at 355 and 532 nm, and the Angström exponent for extinction for specific aerosol types. The *a priori* assumptions are derived from GOCART (Chin et al., 2002). The impact of these optimized constraints is studied using numerical simulations. The optimized constraints are applied to the inversion of experimental measurements acquired by the NASA LaRC HSRL-2 airborne lidar system (Hair et al., 2008) that operated during the NASA Deriving Information on Surface Conditions from COlumn and VERtically Resolved Observations Relevant to Air Quality (DISCOVER-AQ) field campaigns. DISCOVER-AQ was held in Baltimore-Washington D.C. (2011), California (2013), Houston (2013) and Denver (2014). During DISCOVER-AQ there were also flights with in-situ instrumentation (e.g. Ziemba et al., 2013) that provided measurements of SSA that are used to evaluate the results of the constrained retrieval.

The paper is structured as follows: Section II studies the constraints in the retrieval of aerosol microphysical properties. Section III is devoted to the computation of optimized, case-dependent constraints in the stand-alone 3β+2α lidar inversion. Section IV presents the results of applying optimized constraints to stand-alone 3β+2α lidar inversion for HSRL-2 measurements and an intercomparison of these retrievals with airborne in-situ measurements. Conclusions are given in section V.

2.- Study of constraints for the 3β+2α lidar inversion

2.1- Solution of ill-posed problem by regularization: optimized constraints

The extinction and backscattering properties of an ensemble of polydisperse aerosol particles interacting with radiation are related to the particle volume distribution (v(r)) via Fredholm integral equations as (Müller et al., 1999a,b; Veselovskii et al., 2002):

$$g_j(\lambda_i) = \int_{r_{min}}^{r_{max}} K_{j,V}(m,r,\lambda_i)v(r)dr \qquad (1)$$

where 'j' corresponds either to extinction (α) or backscattering (β). Optical data are $g_j(\lambda_i)$ at wavelength λ_i, and $K_{j,V}(m,r,\lambda_i)$ are the volume kernel functions (backscatter or extinction) that depend on particle radius 'r' and complex refractive index $m = m_r + im_i$ at the corresponding wavelength 'λ'.

To solve equation 1, the well-known regularization technique (e.g. Müller et al., 1999a,b; Veselovskii et al., 2002) can be used. The technique as implemented here uses a linear combination of basis functions (triangular in form) to reconstruct the size distribution and identifies a group of solutions that provides a realistic estimation of particle parameters. Such identification can be done by limiting the range over which a solution is sought and by considering the discrepancy (ρ), defined as the difference between the input optical data $g(\lambda)$ and the $g'(\lambda)$ calculated from the set of solutions. As the inversion problem is underdetermined and thus many solutions are possible, to stabilize the inversion an averaging procedure is used that selects a set of solutions in the vicinity of the minimum discrepancy (Veselovskii et al., 2002, 2004). Typically, the average of approximately 1% of the total number of solutions is used as the best estimate of the particle parameters. In this work, spherical particles are assumed and the Mie theory (Mie, 1908) is used. Spherical particles typically include a wide set of aerosols such as pollution, biomass-burning or sea salt (e.g. Dubovik et al., 2002). The study of non-spherical particles such as dust is possible with the adaptation of AERONET kernel functions (Veselovskii et al., 2010), but is beyond the scope of this study.

Retrievals of aerosol refractive index by regularization currently claim uncertainties of ± 0.05 for m_r and around ±100 % for m_i (Müller et al., 1999a,b; Veselovskii et al., 2002, 2004). For other parameters such as effective radius (r_{eff}) and particle volume concentration (V) uncertainties claimed are around 30% and 25% respectively (e.g. Veselovskii et al., 2002; Whiteman et al., 2018). But all these previous works constrained the inversion to a maximum imaginary refractive index ($m_{i,max}$) of 0.01 which is a limitation in the retrieval of refractive index and consequently for the retrieval of aerosol absorption properties.

Limiting the value of refractive index allowed in the inversion, both real and imaginary parts, improves retrieval results, particularly if the allowed values are close to the real ones. But ideally the inversion should be able to retrieve refractive index with no limitations, as is the case for the AERONET inversion methodology. Here, due to the limited information content of the $3\beta+2\alpha$ configuration we perform simulations to better understand the impact of limiting the allowed range of refractive index in the inversion. In the simulations optical data (backscattering and extinction coefficients for the $3\beta+2\alpha$ configuration) are generated for unimodal size distributions with modal radius (r_{fine}) of 0.075, 0.10, 0.14 and 0.18 μm and width (σ) of 0.4 μm. Refractive indices used in the simulations vary with $m_{r,truth}$= 1.35, 1.45, 1.55 and 1.65 and $m_{i,truth}$= 0.001, 0.005, 0.01, 0.015, 0.02, 0.025, 0.03 and 0.05. The use of these ranges permits different magnitudes of absorption to be included. The optical data corresponding to the given size distribution and the various combinations of refractive indices were computed using Mie theory and then used as input to the inversions. No errors in the optical data are assumed at this stage. The inversions then provided the retrieved aerosol refractive indices, both real ($m_{r,retrieved}$) and imaginary ($m_{i,retrieved}$), and also aerosol bulk parameters such as effective radius ($R_{eff,retrieved}$) and volume concentration ($V_{retrieved}$). But the inversions were run in two different ways: one using traditional constraints that implies m_r ranging from 1.35 to 1.65 and m_i maximum value ($m_{i,max}$) of 0.1. The second consisted of applying tightened, case-dependent, constraints that limit refractive index variability around the true value, with m_r ranging from $m_{r,truth}$– 0.1 to $m_{r,truth}$ +0.1 and $m_{i,max}$= 2.5$m_{i,truth}$. In both approaches, steps in m_r are 0.025 and in m_i 0.001. The maximum value of radius of the size distribution allowed in the inversion is 2 μm which is appropriate for predominance of fine particles (Pérez-Ramírez et al., 2013). Figure 1 summarizes the main results of all retrievals. It shows the differences versus the imaginary refractive index used for the simulations. The data are plotted for the different sets of $m_{r,truth}$ and we represent mean values and standard deviations for the four different values of r_{fine}. Dashed black lines represent the uncertainties in the bulk parameters and in the refractive index claimed in the bibliography (Müller et al., 1999a,b; Veselovskii et al., 2002).

[Insert Figure 1 here]

Figure 1a-b shows the differences between retrieved and truth real refractive index as a function of $m_{i,truth}$. Using the traditional constraints, the only cases within the allowed uncertainties are for $m_r = 1.55$ when $m_{i,truth} < 0.01$ and for $m_r = 1.45$ when $m_{i,truth} > 0.01$. However, a clear improvement is observed when using tightened constraints with all the differences within the uncertainties. For imaginary refractive index (Figures 1 (c)-(d)), it is clearly observed that with traditional constraints differences in m_i are above uncertainties for low values of $m_{i,truth}$, particularly for $m_{r,truth}$ of 1.35 and 1.45. However, when tightened constraints are applied all mean differences are within the uncertainties, even though we observe slight departures when standard deviations are included for very small values of $m_{i,truth}$. The improvement in m_i retrieval is clear when tightened, case-dependent, constraints are applied and can be clearly observed as uncertainties are reduced to ~50%. The use of tightened constraints is also critical to reduce the standard deviations of the retrieval and the variability of the differences with $m_{r,truth}$.

Figure 1 (e)-(f) shows the differences in effective radius and again an improvement is observed in the retrievals using tightened constraints, particularly for $m_{i,truth} > 0.01$ and for $m_{r,truth}$=1.35 and 1.65. But here the improvement is not so critical as for refractive index and we remember that the retrieval of effective radius was constrained to r_{max} = 2 μm which is suggested as appropriate when dealing only with fine mode particles. Similar results are observed for volume concentration (Figure 1 (g)-(h)).

The overall conclusion from Figure 1 is that if the real and imaginary refractive indices can be constrained tightly, a significant improvement in the retrieval of the aerosol refractive index from the 3β+2α lidar inversion is obtained. Particularly, when m_r is constrained to within $m_{r,truth}$ ± 0.1 and m_i is constrained to $m_{i,max}$= 2.5$m_{i,truth}$, then retrievals are within the allowed uncertainties. We also repeated the simulations with a larger permitted range of values for both m_r and m_i. Specifically m_r was permitted to range over $m_{r,truth}$ ± 0.15 and m_i varied either up to $m_{i,max}$ = 5$m_{i,truth}$ or $m_{i,max}$ = 7.5$m_{i,truth}$ In all of these tests we observed that the tighten constraints produced better retrievals . Therefore, the simulations presented here indicate that the tighten constraints of m_r within $m_{r,truth}$ ± 0.1 and m_i ranging up to $m_{i,max}$= 2.5$m_{i,truth}$ produce significantly improved inversion results while allowing a range of physical results to occur. But because we do not know generally the input aerosol refractive index from experimental measurements we need to develop a proxy such that we can establish tightened constraints. To develop that proxy, we now study the AERONET database of retrievals.

2.2- Study of AERONET retrieved refractive indices and single scattering albedo in support of the stand-alone 3β+2α lidar inversion.

The AERONET inversion algorithm provides only column-integrated values but the large number of measurements of good accuracy increases the information content of the inverse solution which minimizes the differences between input and computed radiances by the forward model using the retrieved aerosol size distribution and refractive indices (Dubovik and King, 2000). AERONET assumes constraints in smoothing the retrievals and in assuming that complex refractive index is the same for all particles (Dubovik et al., 2000, 2006). However, AERONET is considerably less restrictive in the range of refractive indexes allowed in the inversions than in the lidar inversion technique. AERONET also assumes limits on the ranges of retrieved parameters but again is less restrictive than the tightened constraints discussed in the previous sections.

For the cases of pollution and biomass-burning, which have mostly fine mode predominance for which the spherical particle assumption is reasonable, several worldwide AERONET stations are selected and we use only retrievals whose retrieved sphericity parameter is larger than 70 %. The stations selected are reported in Table 1 and they are representative of different polluted areas in Asia, America and Europe. Also, stations typically affected by biomass-burning aerosol are included. The large number of stations selected allows the inclusion of sites with very different aerosol fine mode characteristics and we believe they are reasonably representative of the many types of fine-mode aerosol present in the atmosphere.

[Insert Table 1 here]

Table 1 shows the main statistical parameters of the retrieved refractive index and SSA (mean, standard deviation and maximum and minimum value) at the reference wavelength of 532 nm – typical of lidar retrievals – determined from a linear interpolation of retrieved values at 440 and 670 nm. Measured aerosol optical depths (AOD) and Ångström parameter (computed from AOD measurements in the range 440-870 nm), and retrieved effective radius (r_{eff}) are also included – note that these parameters are only given for the cases when SSA is retrieved, which requires that AOD(440nm) > 0.4 (Holben et al., 2006). Table 1 data cover biomass burning and pollution in various mixtures, and allow robust representation of aerosol absorption including cases with a large range of refractive index and SSA.

Table 1 reveals spatial variability in aerosol absorption properties, with higher absorption observed in Asia and Latin America than in Europe and North America. Carbonaceous species are highly absorbing and their variability could be the reason for the observed differences in absorption at polluted sites (e.g. Eck et al., 2010). Generally mean values of m_r are mostly in the range of 1.4-1.5 with standard deviation of ~ 0.15. These values are typical of polluted and biomass-burning aerosols (e.g. Dubovik et al., 2002; Reid et al., 2005). Minimum values are ~1.33 with maxima ~1.6. Values below 1.40 are rare for these aerosol types and can be due to the uncertainties in the AERONET inversions (± 0.03 or even larger for low AODs (Dubovik et al., 2000)). Nevertheless, aerosols with strong hygroscopic growth characteristics can possess m_r below 1.40 (e.g. Veselovskii et al., 2009 for the Washington D.C. area). The very high values of m_r can be explained by the large presence of carbonaceous particles. All ofthese results indicate a large variability in the scattering properties of these aerosol particles. For m_i, mean values are observed mostly in the range of 0.005 – 0.025 with more variability in the standard deviation than for m_r. Minimum values are very close to zero while the maxima reach values above 0.07. The predominance of fine mode particles is supported by the large Ångström exponents (all mean values are larger than 1.4) and low r_{eff} (all mean values are less than 0.33 μm). The link of m_i to absorption is clear as high m_i values correspond to low SSA – e.g. m_i close to 0.02 mostly yields SSA in the range of 0.85 – 0.90. Nevertheless, there is not a one-to-one relationship between m_i and SSA because SSA is also sensitive to the size of particles and the real refractive index.

Figure 2 presents color density plots of AERONET retrieved real refractive index ($m_{r,AERONET}$) versus imaginary refractive index ($m_{i,AERONET}$). Retrieved parameters are given again at 532 nm. Data used are all of those described in Table 1, with a total of 15,445 retrievals being analyzed. Figure 2 indicates a general increase in $m_{r,AERONET}$ as $m_{i,AERONET}$ increases with significant variability. Nevertheless, some general relationships can be drawn. For the predominately fine mode particle types represented here, when $m_{i,AERONET}$ is less than 0.01, 90% of the $m_{r,AERONET}$ are less than 1.5. For medium absorbing cases (e.g. $0.01 < m_i < 0.04$), 90% of the values of m_r are above 1.40 and below 1.55. For cases with $m_i > 0.04$, 85% of the values of m_r are above 1.5. These general relationships are enough to improve the constraints on the lidar retrieval similar to section 2.1, assuming we are able to infer the aerosol type and absorption regime. We note that the relationships found are limited by AERONET inversion uncertainties and no further conclusions about the relationships of m_r versus m_i from the data of Figure 2 can be obtained.

[Insert Figure 2 here]

2.3-Optimization of the 3β+2α lidar inversion

Aerosol models can be used to roughly correlate aerosol refractive index to different aerosol categories. We do so here using the Goddard Chemistry, Aerosol, Radiation, and Transport (GOCART) model. GOCART provides simulations of major tropospheric aerosols - sulfate, dust, black carbon, organic carbon, and sea-salt. GOCART assumes aerosol to be in an external mixture. In GOCART, sulfate and carbonaceous aerosols are all assumed to be in the fine mode. Sea salt and dust are both represented by a series of five size bins (0.03 – 10 μm dry radius for sea salt), allowing for simulation of both the fine and coarse fractions of each. Sea salt, sulfate and carbonaceous species are carried as bulk mass tracers with additional partitioning between hydrophobic and hydrophilic modes. Table 2 summarizes the main properties of the aerosol species assumed as spherical particles in GOCART. Note that dust is assumed to be non-spherical and therefore not included in our analyses here. Detailed descriptions of the model are in (Chin et al., 2000, 2002, 2004; Ginoux et al., 2001).

[Insert Table 2 here]

The GOCART aerosol model is used in this analysis to study the coherence of the relationship found in the previous section between m_r and m_i using the AERONET almucantar retrievals and consequently to determine optimized constraints on both aerosol size and absorption in the retrievals. For cases with fine mode predominance, relationships between m_r and m_i in GOCART agree with that observed in Figure 2 from AERONET almucantar inversions. For fine mode particles GOCART suggests large variability in absorption levels: low absorbing particles (e.g. $m_i < 0.01$) are mainly associated with sulphates and/or highly hydrated carbonaceous species and typically have m_r below 1.5, which agrees with observed in Figure 2 for $m_{i,AERONET} < 0.01$. High absorption (e.g. $m_i > 0.04$) is assumed in GOCART to be only associated with cases possessing a significant amount of black carbon which implies $m_r > 1.5$ as indicated by Figure 2 as well. Considering medium absorbing cases (e.g. $0.01 < m_i < 0.04$) with a fine mode predominance, in GOCART are found either a mixture of absorbing carbonaceous species and sulfates, or just carbonaceous species partly affected by hygroscopic growth. For these medium absorbing cases in GOCART, m_r is found to have mean values between 1.425-1.525, in good agreement with Figure 2 where a mean value of 1.47 was found for this interval of m_i and 90% of the values of m_r are above 1.40. Finally, we note that GOCART assumes a size distribution whose width does not change with relative humidity, which is a strong assumption but not critical in the objective of determining optimized constraints in the stand-alone 3β+2α lidar inversion.

GOCART is also used to understand the constraints in refractive index for coarse mode predominance and their mixtures with other fine-mode particles. Actually, for the cases of coarse mode predominance only sea salt particles are included in our analysis using GOCART (dust is excluded because is assumed non-spherical). Sea salt is non-absorbing (see Table 2) and we can assume $m_{i,max}$= 0.001 for the retrievals. Also, for coarse mode we need to allow large variability in m_r due to the large variability of this parameter for sea salt particles. For mixtures of both fine and coarse, however, GOCART indicates more variability in m_i: Mixtures of sulphate and/or hydrated particles with sea salt typically possess m_i below 0.01, while when we include dry carbonaceous particles in the mixtures GOCART allows cases with m_i above 0.01. In both cases of mixtures, m_r is typically below 1.5 according to GOCART. Note that cases with m_i above 0.04 are rarely expected because those cases usually are associated with a large presence of carbonaceous species where the contribution of other species such as sea salt is negligible. As before, the hypothesis of constant width in aerosol size distribution in GOCART is not critical for determining optimized constraints for refractive index in the stand-alone 3β+2α lidar inversion.

Due to the lack of information for independent retrieval of the spectral dependence of imaginary refractive index, the optimized constraints for spherical particles assume no spectral dependence in $m_{i.}$ Thus the retrieved aerosol refractive index is given at a reference wavelength at 532 nm only.Despite this, it should be noted that the main absorbing species in GOCART used for defining the optimized constraints are carbonaceous species, for which the spectral dependence of refractive index is relatively mild in GOCART (Chin et al., 2002). AERONET retrievals of m_i in the fine mode are also assumed to be spectrally independent (Schuster et al., 2016a,b). However, more recent investigations indicate that larger m_i values for organic carbon in the UV region are needed to agree with OMI observations (Buchard et al., 2015). This result is important for biomass-burning but not for pollution events (Colarco et al., 2017). For all of these reasons, in the aerosol inversions considered here when spectral dependence in m_i is present additional uncertainties are added to the retrieved parameters. Refractive index in other regions such as the infrared (e.g. Volz, 1973) can follow very different patterns to those used here, but retrievals in these spectral regions is beyond the capability of the stand-alone $3\beta+2\alpha$ lidar technique.

But the selection of the range of radii allowed in the inversion must be done carefully as it can influence the accuracy and sensitivity of the retrievals (e.g. Müller et al., 1999a,b; Veselovskii et al., 2002). Typically only two modes of aerosol particles are assumed for the wavelengths used here: fine mode that corresponds to particles of radius typically below 0.5-0.6 μm, and coarse particles for those with larger radii (Dubovik et al., 2002). For fine mode particles the radii permitted in the inversion are in the range of 0.075 and 2 μm. For coarse mode predominance, the maximum radius permitted in the inversion is increased to 10 μm and the minimum radius also increases to ~ 0.2μm. Finally, for a mixture of fine and coarse particles the inversion is evaluated over the entire range of 0.075 to 10 μm. Therefore, we need to look for a method that is able to provide optimized constraints both in refractive index and in the range of radii.

We note that other species such as nitrates are also present in the atmosphere and are particularly prevalent in polluted regions (e.g. Wang et al., 2010). Nitrates are highly hygroscopic (e.g. Tang, 1996), low absorbing (e.g. Toon et al., 1994; Richwine et al., 1995;

Norman et al., 1999), and for our wavelengths of interest (355, 532 and 1064 nm) have real refractive indices that are similar to sulphates, both from laboratory (e.g. Toon et al., 1994; Richwine et al., 1995) and in-situ measurements (Zhang et al., 2012). The optical properties for fine mode sulphate particles are already included in Table 2 so it is not necessary to consider nitrates in defining optimized constraints. On the other hand, nitrates can also interact with sea salt and dust and modify the optical properties of coarse particles. But for coarse particles and their mixtures, we did not find any relationship between m_r and m_i as for the smaller particles although, still, we found it beneficial to limit the maximum value of mi as before. Because in mixtures of fine mode particles low absorbing aerosol is represented by either sulphates, sea salt or hydrated aerosols it is not necessary to include nitrates.

3.-Optimized constraints for the stand-alone 3β+2α lidar inversion

3.1- Computation of optimized constraints

To establish the set of constraints for the stand-alone 3β+2α lidar inversion we need first to determine the range of radii for the inversion, noting that the Angstrom exponent of extinction (γ_α) is strongly correlated to particle size (e.g. Dubovik et al., 2002). To understand the relationship between Angstrom exponent and PSD, computations were made of γ_α for different sets of unimodal size distributions with r_{fine} =0.10, 0.14, 0.18, 0.25, 0.3, 0.4, 0.5, 0.6, 0.8, 1.0, 1.5 and 2 μm with σ_M =0.4 μm. Computations for bimodal size distributions are also included with fine mode at r_{fine} = 0.14 μm and σ_{fine} =0.4 μm, coarse mode at r_{coarse} = 1.5 μm and with σ_{coarse} =0.6 μm and V_f/V_c of 2, 1, 0.5, 0.2 and 0.1. Refractive indices used were m_r = 1.35, 1.45, 1.55

and 1.65 and m_i = 0.001, 0.005, 0.01, 0.02, 0.025, 0.03, 0.04, 0.05, 0.075 and 0.1. Figure 3 shows γ_α as a function of r_{fine} of the unimodal size distributions used as input. For clarity, only those at m_r =1.35 and m_r = 1.65 are shown. Black dots are for bimodal size distributions where the error bars represent the standard deviation associated with m_r variability.

[Insert Figure 3 here]

From Figure 3 all data for γ_α>1.25 are associated with a large predominance of the fine mode (r_{eff}< 0.3 um), independently of m_i values. However not all cases dominated by fine mode have such large values of the γ_α. Some cases dominated by fine mode particles, specifically those with m_i> 0.03, have low to intermediate values of γ_α. Therefore, only high values of γ_α (>1.25) correspond unambiguously to the specific size category of fine mode predominance. Other cases require more information and further analysis to categorize. We also note that this analysis is for the γ_α computed using 355 and 532 nm used in the 3β+2α lidar configuration.

The extinction-to-backscatter ratio (lidar ratio, or LR) is studied here because it is a parameter related both to particle size and refractive index. Computations of LR at 355 and 532 nm were done assuming Gaussian and unimodal aerosol size distributions, which can be representative of a PSD consisting of only fine mode particles (e.g. Dubovik et al., 2002). The computations were done for different sets of r_{fine} of 0.075, 0.10, 0.14 and 0.18 µm – guaranteeing only fine mode particles - and m_i of 0.001, 0.005, 0.01, 0.025, 0.05 and 0.075. The width of the size distribution (σ) is fixed in all computations to σ = 0.4 µm. Figure 4 shows the spectral dependence of LR: continuous lines represent fixed r_{fine} and variable m_i, while dashed lines imply fixed m_i and variable r_{fine}. Initially, we selected four representative values of m_r that cover most aerosol particles, 1.35, 1.45, 1.55 and 1.65, but for simplicity only results for m_r = 1.45 (red lines) and m_r = 1.65 (black lines) are shown. Data used to build Figure 4 are given in Table 3.

From the plots of Figure 4 the limiting value of the imaginary refractive index used in the inversion can be estimated (m_i') by linear interpolation, but this selection depends on the assumed m_r and therefore more analyses are needed for an appropriate estimation of imaginary refractive index. We remark that additional computations were done for other widths of the size distribution (graphs not shown for brevity), σ = 0.2 and 0.6 μm representing lower and higher typical values for fine mode predominant distributions, and we observe the same patterns as in the plots of Figure 4, with only slightly broader plots for σ = 0.2 μm and slightly narrower plots for σ = 0.6 μm. Therefore the assumption of size distribution width can lead to small differences in the computation of m_i using the graphical method of Figure 4, but given that the graphical method is designed to provide optimized constraints on the inversion these differences in σ do not significantly influence the $3\beta+2\alpha$ inversion results.

[Insert Figure 4 here]

[Insert Table 3 here]

Figure 5 shows the dependence of the ratio of LR for 355 and 532 nm values (LR(355)/LR(532) - hereafter LR_{ratio}) as a function of γ_α. In these plots m_i is now fixed and representative plots for low (e.g. m_i =0.005) and medium absorption (e.g. m_i =0.025) are shown, respectively. The plots are computed again for the same sets of r_{fine} (0.075, 0.10, 0.14 and 0.18 μm) and fixed σ = 0.4 μm but now varying the different values of m_r: 1.35 (green lines), 1.45 (red lines), 1.55 (blue lines) and 1.65 (black lines). Data for Figure 5 are given in Table 4. Figure 5 clearly reveals relationships between LR_{ratio} and γ_α, and suggests that such graphs can be used as proxy to estimate the limiting value of real refractive index (m_r') by linear interpolation. Such estimated value is used to verify the ranges of m_i' that were previously determined in Figure 4 but not as a final retrieved value

[Insert Figure 5 here]

[Insert Table 4 here]

Using the measured 3β+2α values and Figures 4 and 5, the step-by-step graphical method for determining a coarse estimation of refractive index m_i' is as follows:

1. We determine typical values of $m_r^{(k)}$ covering the different ranges observed in the bibliography. Taking into account the uncertainties of m_r in the lidar retrievals of ± 0.05 we have selected $m_r^{(1)} = 1.35$, $m_r^{(2)} = 1.45$, $m_r^{(3)} = 1.55$ and $m_r^{(4)} = 1.65$ as representative. The superscript '*k*' corresponds to each of the four assumed m_r as input.

2. From the measured 3β+2α the corresponding LR(355 nm) and LR(532 nm) is computed and using the graphical method of Figure 4 we determine each value of $m_i^{'(k)}$.

3. We calculate γ_α from the measured extinction coefficients and using $m_i^{'(k)}$ obtained in step 2 we compute the four graphs LR(355 nm)/LR(532 nm) versus γ_α (graphical method of Figure 5). For each of these plots we interpolate and obtain an estimated value of real refractive index, denoted $m_r^{'(k)}$. For each '*k*' value, If the difference $m_r^{(k)} - m_r^{'(k)}$ is larger than ±0.05 then the corresponding $m_i^{'(k)}$ is rejected. The reason behind the rejection is that the measured LRs and γ_α do not correspond with a size distribution and refractive index under the hypotheses used to build both Figures 4 and 5. But there could be cases where only some ´*k*´ values are rejected while others fulfill the hypothesis of size

distributions and refractive index of Figures 4 and 5 – e.g. for $m_r^{(1)}$ = 1.35 the estimated $m_i^{'(1)}$ might be rejected while for $m_r^{(3)}$ = 1.55 the estimated $m_i^{'(3)}$ is valid.

4. The final value of m_i’ is computed as the average of the $m_i^{'}(k)$ values computed without rejection. The estimated m_i’ is used to compute $m_{i,max}$= 2.5m_i’ (section 2.1) and also using the relationships found in Figure 2 are used to estimate m_r’, which serves to define the range of allowed m_r in the inversion as m_r’ ± 0.1.

5. Considering now Figure 3, $\gamma_\alpha < 1.25$ could correspond either to fine mode predominance with strong absorption (e.g. m_i> 0.03) or size distribution with mixture of fine and coarse particles. But the graphical method of Figures 4 and 5 is based on the assumption of fine mode predominance, sofrom measured 3β+2α with γ_α<1.25, if the four m_i^k were rejected in step 3, these cannot correspond to a predominance of fine mode and therefore must correspond either with a predominance of coarse mode particles or with a mixture of fine and coarse modes.

For these cases, according to the GOCART background (section 2.2), spherical coarse particles correspond with sea salt particles having low refractive index. In the AERONET retrievals a residual coarse mode is observed in biomass-burning or polluted cases affected by hygroscopic growth or other aging process. The particles that fall in the area of separation between fine and coarse mode could induce an artifact in the retrieval and explain the residual coarse mode in biomass-burning. In any case, with the limitations assumed here of the same refractive index for both modes we can assume that in the mixture of particles no very high values of m_i are observed because such cases corresponds to a large contribution of dry carbonaceous particles and therefore of fine particles. Under these assumptions simulations were done for bimodal size distributions (r_{fine} = 0.14 μm, σ_{fine} = 0.4 μm, r_{coarse} = 1.5μm, σ_{coarse} = 0.6 μm), where the ratio of volumes between both modes varies from 2 to 0.1. The same set of refractive indices as in Figure 4 are assumed but with m_i up to 0.04. Figure 6 shows the spectral dependence of LR for m_r = 1.55, which can be assumed as illustrative of a mixture of particles where it is possible to have large m_i (e.g. dry carbonaceous and sea salt typically do possess m_r between 1.50 and 1.60 – Table 2). The data to build Figure 6 are given in Table 5 and again Figure 6 allows a direct coarse estimation of aerosol imaginary refractive index.

[Insert Figure 6 here]

[Insert Table 5 here]

There are other possible mixtures of particles with different values of m_r – e.g. cases with large hygroscopicity or with important contribution of sulphate particles (Table 2). But according to GOCART these cases possess m_i below 0.01, and therefore we limited the computations to m_i = 0.01. In Figure 6 we also include the plot for m_r = 1.35 as representative of alternative cases, and we observe that all the data of these new plot fall in the region corresponding to m_i< 0.01 for the plot computed for m_r = 1.55, and therefore we conclude that the plot for m_r = 1.55 can be used as representative of most mixtures.

The graphical method of Figure 5 for m_r = 1.55 is used to compute m_i' when the aerosol size distribution is suggested as a mixture of fine and coarse modes in step 5, and we can therefore compute $m_{i,max}$= 2.5m_i' which is later used in the 3β+2α inversion. However, for mixtures, the relationships between m_r and m_i from AERONET retrievals (Figure 2) are not representative and due to the large variability observed in GOCART for mixtures we do not assume any limitations in the range of m_r allowed in the retrievals. These issues, together with the larger range of radius allowed in the inversion, induce larger errors in the retrievals when a mixture of particles predominates, but agrees with the largest uncertainties associated with these types of particles generally found for the retrievals of aerosol microphysical properties (e.g. Perez-Ramirez et al., 2015).

3.2.- Impact of the optimized constraints in the retrievals of single scattering albedo

The impact of the optimized constraints in the retrievals of aerosol single scattering albedo (SSA) by the stand-alone 3β+2α lidar is studied here through different simulations: the same hypotheses of the input size distribution as in Figure 1 are used – unimodal size distribution with r_{fine} = 0.075, 0.10, 0.14, and 0.18 μm and with σ = 0.4 μm. Refractive indices used in the simulations vary with $m_{r,truth}$ = 1.35, 1.45, 1.55 and 1.65 and $m_{i,truth}$ = 0.00, 0.001, 0.005, 0.01, 0.025, 0.05, 0.075 and 0.1. The computation of single scattering albedo on the particle size distribution and refractive index and is thus wavelength dependent. Even though we assume a flat spectral dependence of the refractive index, it is nonetheless valuable to study the optimized inversion for retrieval of SSA at different wavelengths.

Figure 7 shows the differences in SSA between retrieved ($SSA_{retrieved}$) and modeled (SSA_{truth}) values of SSA as a function of $m_{i,truth}$. Again, the differences are presented for the traditional constraints with $m_{i,max}$ = 0.1 and where all ranges of m_r are allowed, and for optimized constraints in the retrievals. Results are shown for the four different values of m_r used in the simulations. Shaded areas in the plots of Figure 7 are the uncertainties expected, which are these assumed for AERONET. Actually, AERONET uncertainties claimed for SSA are approximately ±0.02 (e.g. AERONET retrievals in Dubovik et al., (2000)). This uncertainty in SSA for low absorbing aerosol (e.g. SSA > 0.9 and m_i typically below 0.01) implies approximately 20%

uncertainty in the absorption coefficient. For lower SSA (and consequently larger m_i) 20% uncertainties in the absorption coefficient allows larger uncertainties in SSA. Therefore, we allowed these larger uncertainties but keeping the 20% uncertainty in the consequently retrieved absorption coefficient. This effect explains the different shaded areas of Figure 7.

[Insert Figure 7 here]

Figure 7 clearly reveals that optimized constraints are able to reduce the differences between model and retrieved SSA. Optimized constraints are particularly critical in the retrieval of SSA for $m_i < 0.01$. Actually, the optimized constraints are also needed for reducing uncertainties in larger m_i as shown by the improved retrieved values for $m_r = 1.35$ and $m_r = 1.45$. Note though that when the optimized constraints are applied, the differences in SSA fall within the acceptable uncertainties for 355 and 532 nm in all ranges of absorption, while for 1064 nm this does not happen for low absorption that illustrates the difficulty of retrieving very small values of SSA .

For the cases involving a mixture of modes simulations were again done to study the impact of optimized constraints. Now, a bimodal size distribution is used for computing the input $3\beta+2\alpha$ optical data, with fine mode at $r_{m,fine} = 0.14$ μm and $\sigma_{fine} = 0.4$ μm, and coarse mode at $r_{m,coarse} = 1.5$ μm and with $\sigma_{coarse} = 0.6$ μm. The ratio of fine and coarse mode volumes (V_f/V_c) takes values of 2, 1, 0.5, 0.2 and 0.1. The same ranges of refractive index as in Figure 7 are used – although we skipped $m_{i,truth} = 0.075$ and 0.1 because according to GOCART such refractive indices are very rare for mixtures of fine and coarse mode. The under-determined problem requires us, as previously stated, to assume the same refractive indices for both fine and coarse modes, which is also assumed in the current operational AERONET algorithm (Dubovik and

King, 2000). Figure 8 shows the dependence of the differences between retrieved and model SSA as function of imaginary refractive index. Because the differences are computed for all the different values of m_r and m_i, we represent in Figure 8 absolute values of these differences with the error bars showing the standard deviations associated with the different input m_r in the simulations. Also, for clarity we show differences when no limitations in the range of m_r and with $m_{i,max}$ = 0.1 (labeled as 'traditional constraints' in the plot). For the inversions with optimized constraints we show two cases for clarity, one for cases when $m_{i,model}$< 0.01 (labeled as 'low absorption') and the other with $m_{i,model}$> 0.01 (labeled as 'medium absorption').

Figure 8 reveals again that optimized constraints are critical for the retrieval of SSA in the cases of mixtures of particles, both for low and medium absorbing particles. However, now important results are observed with wavelengths and with the contribution of each mode: for 355 nm, SSA retrievals fail as the coarse mode becomes more relevant, which is clearly seen for V_f/V_c< 1, indicating a critical limitation of the retrieval. Actually, it is observed that for V_f/V_c< 1 the optimized constraints do not produce significant improvements in the retrievals. However, for 1064 nm, now retrievals of SSA are possible and optimized constraints are only critical for cases with m_i< 0.01.

At 1064 nm we note that the use of optimized constraints are not as critical as for the other wavelengths, although the deviations are always ~0.04 when no constraints are used and therefore above the uncertainties mainly for low absorbing cases. Nevertheless, the large standard deviations observed suggest to always use optimized constraints. We also remark that the degradation of the retrieval with V_f/V_c for optimized constraints is not as critical as for 355 nm, although differences are only below the allowed uncertainties for V_f/V_c< 1.0.

For 532 nm, an intermediate result between those of the previous wavelengths is observed. The improved capabilities of the inversion for retrieving SSA at 1064 nm versus 355 or 532 nm for coarse mode predominant cases is expected as the interaction of light with big particles becomes more effective at 1064 nm, while the opposite occurs at 355 nm.

[Insert Figure 8 here]

The conclusion from all these simulations is that optimized constraints are critical for the stand-alone $3\beta+2\alpha$ lidar inversion for retrieving SSA. But also there are limitations relating to the dominant particle size. For fine mode particle predominance, such as for fresh biomass burning or pollution cases, reliable retrievals are only possible in the ultraviolet and visible regions. As the coarse mode increases, retrieved SSA at 1064 nm becomes possible while retrievals lose their capabilities in the ultraviolet region. Actually, for mixtures of particles SSA retrievals at all wavelengths are only possible when the contribution of fine particles is significant ($V_f/V_c < 1$), which for real aerosol can happen for aged cases of smoke and pollution that possess a residual coarse mode (Dubovik et al., 2002).

4.- Experimental Results

4.1- Instrumentation and Methodology used.

During DISCOVER-AQ the NASA Langley second-generation airborne HSRL-2 system was deployed from the NASA LaRC King Air B200 aircraft on California, Texas and Colorado field campaigns, and obtained over 300 science flight hours. The typical flight altitude of the

B200 during lidar operations was 9 km. The system uses the High Spectral Resolution Lidar technique (HSRL - Shipley et al., 1983) to independently measure aerosol extinction and backscatter at 355 and 532nm and the standard backscatter technique (Klett 1981, 1985: Fernald, 1984) to measure aerosol backscatter at 1064nm. Preliminary work with DISCOVER-AQ data indicated the capabilities of HSRL-2 to evaluate hybrid-retrievals (e.g. Sawamura et al., 2014) and bulk parameters of the stand-alone $3\beta+2\alpha$ lidar inversion (Sawamura et al., 2017), and here HSRL-2 measurements are used to evaluate SSA retrievals. The system also measures linear depolarization ratio (δ) at all three wavelengths (Burton et al., 2015). HSRL-2 is a follow-on to the successful airborne HSRL-1 instrument (Hair et al., 2008), which has made measurements at 532 and 1064 nm since 2006 (Rogers et al., 2009). The novelty of HSRL-2 is the capability to measure independent extinction and backscattering at 355 nm (Burton et al., 2018). The system is able to acquire measurements at 0.5 s temporal and at 7.5 m vertical resolutions. Aerosol backscatter and depolarization products are averaged for 10 s (yielding a horizontally resolution of ~ 1 km at nominal aircraft speed) and aerosol extinction products are averaged for 60 s (~ 6 km). The optical data used here are available on the DISCOVER-AQ data archive at http://www-air. larc.nasa.gov/missions/discover-aq/discover-aq.html.

For aerosol typing using aerosol intensive parameters including spectral δ, lidar ratio, and backscatter Angstrom exponent, the algorithm used is described in Burton et al., (2012, 2013, 2014) and is able to separate between: ice (specifically small diameter arctic ice fog particles that are not separately cleared as cloud in the HSRL algorithms) (1), dusty mix aerosol (2), maritime aerosol (3), urban/pollution aerosol (4), smoke (5), fresh smoke (6), polluted maritime aerosol (7), and pure dust (8). Since not every set of measurements can be unambiguously typed to one specific class, the code (9) indicates points that are unclassified because they are consistent with more than one class. We note that aerosol classification is presented as qualitative and the accuracy can be affected by a variety of common circumstances such as aerosol which is not consistent with the set of training cases used (e.g. differences in ‘urban’ aerosol between western and eastern US – Burton et al., 2012, 2014). Mistyping for classes that have similar values in the observables used for classification can also be the cause of inconsistencies in aerosol typing (e.g. smoke of forest or agricultural are sometimes hard to separate from urban aerosol – Burton et al., 2012, 2014).

The NASA P-3B aircraft acquired in-situ measurements of aerosol properties during the DISCOVER-AQ field campaigns. Sampling was done through an isokinetic, low-turbulence inlet which transmits particles smaller than 5 µm diameter with greater than 50% efficiency (McNaughton et al., 2007). A limitation of typical in-situ instrumentation is that it dries the particle and therefore, the measured values are not representative of those in the real atmosphere. To circumvent this limitation, during the DISCOVER-AQ campaign, both dry and humidified scattering coefficients (450, 550, and 700 nm wavelengths) were measured with a pair of integrating nephelometers (Model 3563, TSI, Inc., Shoreview, MN, USA) (Pilat and Charlson, 1966; Clarke et al., 2002). The measurements were corrected for truncation errors following Anderson and Ogren (1998). One nephelometer operated at dry relative humidity (RH_{dry}~ 10%), while the other operated at high relative humidity (RH_{wet}~ 80-85%). Combining the measurements from both instruments permits calculation of the aerosol hygroscopicity parameter (χ), which is related to the ratio between extinction coefficients at RH = 80 % and at RH = 10%. Computation of scattering coefficients at ambient conditions is done following Ziemba et al., (2013). The scattering Ångström exponents are used to obtain scattering coefficients at 532 nm. Dry aerosol absorption coefficient (470, 532, and 660 nm wavelengths) is obtained from a

Particle Soot Absorption Photometer (PSAP; Radiance Research, Shoreline, WA, USA), whose measurements are corrected for filter artifacts following Virkkula (2010). Hygroscopic growth effects on absorption coefficients were neglected. The final aerosol extinction coefficient at ambient temperature is given as the sum of hydrated scattering and absorption coefficients, and through the ratio of hydrated scattering and extinction coefficients SSA at ambient conditions is computed. The P-3B data used are publicly available on http://www-air.larc.nasa.gov/missions/ discover-aq/ discover-aq.html.

Co-incident data of HSRL-2 and P-3B were used with the limitation of maximum 15 km distance between both airplanes. For the match-up, HSRL-2 data were averaged over 75 m altitudes and 1.5 minutes temporal (~ 15 km horizontal equivalent) resolution. The P-3B flew spiral patterns with diameters of 6-10 km and an average vertical resolution of 5 m. For the stand-alone $3\beta+2\alpha$ lidar inversion we imposed a maximum value in depolarization of 5%, consistent with spherical particles, as all our analyses presented here are based on Mie theory. The total numbers of correlative spirals were approximately of 90, 150 and 70 for the California, Texas and Colorado field campaigns, respectively. The total number of correlative points for SSA intercomparisons was 1270, including situations of fine mode predominance and mixture of modes, with cases of m_i estimated varying between 0.001 and 0.03. No cases of very high absorption (e.g. $m_i > 0.05$) were registered.

4.2- Experimental measurements and retrievals of single scattering albedo vertical-profiles

Figure 9 shows the flight tracks of the NASA B200 airplane (in which the HSRL-2 was installed) for three different days during DISCOVER-AQ in California (2013), Colorado (2014) and Texas. Each day is representative of different aerosol conditions. The flights tracks can be found at the DISCOVER-AQ website (https://www-air.larc.nasa.gov/missions/discover-aq/discover-aq.html).

[Insert Figure 9 here]

4.2.1. – San Joaquin Valley: Fine mode and low absorbing aerosol study case

Measurements of aerosol vertical-profiles of α(532) on 30th January 2013 over the San Joaquin Valley are given in Figure 10. Vertical white lines indicate correlative spirals by the P-3B airplane. For this day, backward trajectories were computed by the HYSPLIT model (Stein et al., 2015) and revealed that air masses at altitudes of 1500 and 3500 m. a.g.l. had their origin on the west coast of North America and over the Pacific, and were thus generally very clean (graphs not shown for clarity). For lower altitudes at 500 m a.g.l., the backward-trajectories revealed the presence of local air-masses over the San Joaquin valley. Figure 10a shows no aerosol above the altitude of 1500 m a.g.l., which is consistent with the air-mass patterns and indicates very low planetary boundary layer (PBL) with the presence of local aerosol and pollution. Within the PBL, large relative humidity was registered during most of the measurements (>70%), and mean aerosol hygroscopicity parameter χ of ~ 1.5 obtained by in-situ P-3B instrumentation revealed a large presence of hydrated particles.

Figure 10b shows the results of the aerosol typing using the HSRL-2 aerosol intensive parameters. For the aerosol in the planetary boundary layer no data are classified as dust or dusty mixture consistent with the assumption of spherical particles. Figure10b reveals that most of the aerosol within the PBL corresponds to urban aerosol which agrees with the analyses of backward trajectories mentioned previously. Urban aerosol is more predominant before 20 UTC. Between 18:30 and 19:30 UTC fresh smoke is observed. While the data in this category are probably not always well described by the label “fresh smoke”, the difference in typing nevertheless indicates a change in aerosol optical properties (e.g. Burton et al., 2012, 2013). Between 21 and 24 UTC a presence of marine-polluted aerosol is also observed. Above the PBL are observed some dusty mixtures that possess very low extinction.

All the extinction and backscatter data of Figure 10a within the PBL were used as input to the procedure for computing the optimized constraints of section 3.1. The estimated particle size (fine mode predominance or mixture of modes) and imaginary refractive indexes are given in Figures 10c and 10d, respectively. Particle type is predominantly fine mode that is consistent with the classification of pollution and fresh smoke from the previous typing classification. The estimated m_i is typically below 0.01 with some spikes near the top of the planetary boundary layer ($m_{i,estimated}$~ 0.015). Such low values of estimated m_i are consistent with the presence of fine mode particles from pollution and fresh smoke affected by hygroscopic growth (e.g. Dubovik et al., 2002).

[Insert Figure 10 here]

An example of vertical profiles of aerosol optical and microphysical properties is given in Figure 11 for the 30th January 2013 at 21:54 UTC (GMT-8). Optimized constraints were computed and for all data of the profile fine mode aerosol were present with estimated m_i below 0.01, and therefore the inversions were run under using optimized constraints. Retrieved values of r_{eff} (between 0.10 – 0.15 μm) are typical of fine mode predominance, and V shows a decrease with altitude that agrees with the vertical structure of the extinction measurements. Retrieved values of m_r are approximately 1.40 – 1.475, typical of pollution and hygroscopic aerosol (Veselovskii et al., 2009). The corresponding vertical profiles of SSA obtained by inversion of HSRL-2 lidar measurements and by correlative in-situ airborne measurements are also given in

Figure 11. Retrieved and measured values of SSA are above 0.96 and no vertical structures are observed by any method. Differences in SSA between both methodologies are within the uncertainties.

[Insert Figure 11 here]

4.2.2. – Colorado: Fine mode and medium absorbing aerosol study case

An example of results from DISCOVER-AQ Colorado is given in Figure 12 which shows aerosol vertical profiles of α(532) on 10th August 2014. Different layers are observed with aerosol up to 6 km a.s.l. The PBL is at approximately 3200 m a.s.l.. The analyses of backward-trajectories (graphs not shown for simplicity) reveal that the lower levels below PBL are affected by local air masses that are frequently quite dry for this location. However, the higher levels are affected by air masses with origin in the southeast of the U.S. where several fires were active. Injections of biomass-burning particles in the free troposphere in the South of the US have been observed during the SEACRS field campaign (Reid et al., 2017). Generally southern air masses often contain a high amount of water vapor but the high altitude at which these air masses were transported implied a low amount of water vapor. Actually, the P-3B measurements indicated that hygroscopic growth hardly affected aerosol in these layers, with the increase in size being less than 5 %.

[Insert Figure 12 here]

HSRL-2 measurements of δ indicated that most values for Figure 12 data were below 0.05 guaranteeing again a predominance of spherical particles. The aerosol typing algorithm was again applied (Figure 12b), clearly revealing two different aerosol types: In the PBL urban pollution aerosol is observed while above the PBL smoke is observed. Such patterns agree previous comments concerning backward trajectories. The algorithm of section 3.1 classified most of the data as fine mode predominance (Figure 12c) and estimated m_i between 0.015 and 0.0075 (Figure 12d), in spite of some spikes indicating mixture of particles and suggesting larger m_i in the higher altitudes. These classifications agree with smoke properties that possess fine mode predominance and relatively large imaginary refractive indices (e.g. Dubovik et al., 2002). The mixture of fresh smoke with urban pollution usually possesses large imaginary refractive indices as well (e.g. Eck et al., 2003; Eck et al., 2010).

An example of the aerosol microphysical properties retrieved on 10th August 2014 is given in Figure 13 for data acquired at 15:45 UTC when correlative spirals by P-3B were available. Atmospheric relative humidity measured by the aircraft with in-situ instruments ranged from 55-65%, which implies that aerosols were generally non-hydrated. The $3\beta+2\alpha$ lidar inversion used optimized constraints. Effective radii retrieved were approximately 0.15-0.22 μm, which are typical of pollution and smoke (Dubovik et al., 2002) and indicates fine mode predominance. Actually, these slightly larger values of effective radius compared with these of Figure 11, although within the fine mode, suggest they are close to a mixture and explains the difficulty of the algorithm for selecting the constraints to separate between fine and mixtures and therefore the spikes observed in Figure 12c. The profile of V follows a pattern very similar to the extinction profiles, which is expected as both parameters depend on particle concentrations. The retrieved values of m_r close to 1.55 are again typical of dry pollution and fresh smoke. The retrieved m_i are approximately 0.0075-0.015, which are in the range expected for this type of particles. Retrievals and in-situ measurements of SSA are given with values again of medium absorbing aerosol (~0.92) and differences are within the uncertainties of the method. These retrievals and in-situ measurements suggest relatively significant absorption by these transported smoke particles when they become dry. Unfortunately, only four data were available for intercomparison because the P-3B airplane did not fly at lower altitudes.

[Insert Figure 13 here]

4.2.3. – Houston region: Mixture of particle sizes and medium absorbing aerosol study case

Figure 14a shows an example of aerosol vertical profiles of α(532) on the 26th September 2013 from DISCOVER-AQ Texas in 2013. High PBL is observed with aerosol up to approximately 2300 m a.s.l.. Backward-trajectories were computed again for this day (graphs not shown for simplicity) and revealed air masses with origin in the Midwest of the US that were affected by biomass burning events during the previous days. Measurements by P-3B using the tandem of nephelometers reveal aerosol hygroscopic growth with mean χ of ~1.3. However, the dry air-masses for this day with low relative humidity (~35 – 55 %) did not support aerosol hygroscopic growth in the real atmosphere. Long-range transport of biomass-burning aerosols usually possesses a residual coarse mode and considerable absorption (e.g. Dubovik et al., 2002), and considering the small growth by higroscopicity, these transported particles retained considerable absorption (Pérez-Ramírez et al., 2017).

Again, the presence of spherical particles is mostly indicated by HSRL-2 linear depolarization measurements with values below 0.05, although with some values close to 0.1 that are ignored in the retrievals consistent with the assumption of spherical particles. Figure 14b shows the results of the aerosol typing algorithm. Generally, variability of aerosol types is observed and includes dusty, smoke and polluted maritime aerosols. An overview of all data suggests that mixtures of both coarse and fine mode are predominant as both sea salt and some dust are present in the atmosphere. The algorithm of section 3.1 indicates mostly the predominance of a mixture of particles (Figure 14c) with an estimated refractive index between 0.01-0.02 mostly in the lowest region of the atmosphere (Figure 14d). These types of particles and the range of m_i estimated agree with the mixtures suggested by the aerosol typing. Some spikes near the top of the boundary layer are observed with fine mode predominance and estimated m_i larger than 0.02 that agrees with fresh smoke properties (e.g. Eck et al., 2003) that is also indicated by the aerosol typing.

[Insert Figure 14 here]

Another example of retrieved aerosol properties by the stand-alone 3β+2α lidar inversion with optimized constraints is given in Figure 15 for 26th September 2013 at 20:40 UTC. The retrieved values of r_{eff} between 0.35-0.45 μm are consistent with a mixture of different modes. Retrieved values of m_i between 0.01 - 0.02 and of m_r around 1.55 are also consistent with the mixtures of particles previously mentioned. It is remarkable that the inversions retrieve SSA of up to 0.88 which are confirmed by the correlative in-situ measurements. The larger error bars are due to the significant uncertainties in SSA for large particles and large m_i (e.g. ± 0.04).

[Insert Figure 15 here]

4.2.4. – Overview of lidar vs in-situ instrument on aircraft SSA comparisons

An overview of all SSA intercomparisons between lidar retrieved (SSA_{LIDAR}) and measured by in-situ airplane ($SSA_{IN-SITU}$) can be seen in Figure 16. We represent frequency histograms of the absolute differences SSA_{LIDAR}– $SSA_{IN-SITU}$. Plots are given for four different aerosol conditions registered during DISCOVER-AQ: fine mode predominance and a mixture of modes, and separating for estimated m_i above and below 0.01. During California 2013 all data were classified and evaluated as fine mode predominance and estimated m_i below 0.01, explained by the air-mass patterns typical in the region with origins over the north Pacific at high altitudes and stagnant regimes in San Joaquin valley at low altitudes favoring particles from pollution. For Texas 2013 more variable aerosol conditions were observed, depending on the air-mass pattern and aerosol origin, although the most predominant type is fine mode predominance and estimated m_i above 0.01 with 64.6% of measurements, followed by mixture of modes and estimated m_i above 0.01 with 24.5% of measurements. For the Colorado 2014 campaign different aerosol types were observed depending on air-mass origins, with the most frequent type being fine mode predominance with an estimated m_i above 0.01 (60% of data), followed by fine mode predominance with an estimated m_i below 0.01 (20% of data), while cases of mixtures of modes were less frequent with 10.8 % of data with an estimated m_i below 0.01 and 8.8% of data with an estimated m_i above 0.01. All the data used have linear depolarization measurements below 5%, which indicates essentially spherical particles. A total of 1271 data were used for intercomparisons: fine mode and estimated m_i below 0.01 was the most frequent with 598 cases and mean SSA of 0.97 ± 0.01, ranging from 0.92 to 0.99. Fine mode and estimated m_i above 0.01 is the next highest in frequency, with 502 cases and mean SSA of 0.91 ± 0.03 and ranging from 0.80 to 0.97. Mixture of both fine and coarse modes were the least frequent cases, with a total of 37 cases for estimated m_i below 0.01 (SSA of 0.97 ± 0.01 and ranging between 0.93 and 0.99) and 134 cases for estimated m_i above 0.01 (SSA of 0.90 ± 0.03 and ranging between 0.83 and 0.96).

[Insert Figure 16 here]

Results from Figure 16 indicate that mean SSA differences are zero for fine mode predominance (for any value of estimated m_i) and mixture of modes for estimated m_i above 0.01. The standard deviations differ among the different cases, but taking into account that the inversion constraints approach assumes similar uncertainties in SSA than these from AERONET inversions the standard deviations are within the uncertainties (±0.02 for estimated $m_i < 0.01$ and ±0.04 for estimated $m_i > 0.01$, approximately). For the case of mixture of modes and estimated $m_i < 0.01$ the retrieved SSA systematically overestimates the measured values by 0.02, although the standard deviations are approximately 0.02, thus are within the uncertainty of the method. The difficulty of the inversion to retrieve SSA in the visible range for mixtures of aerosol can explain such differences, although the low number of data available for such cases encourages further evaluations.

5.- Summary, Discussion and Conclusions

The analyses presented in this work have indicated the need for optimized, case-dependent, constraints in the retrievals of aerosol complex refractive index ($m = m_r + im_i$) and single scattering albedo (SSA) from vertical profiles from lidar measurements of three backscattering coefficients (β) at 355, 532 and 1064 and two extinctions (α) at 355 and 532 nm, typically known as the stand-alone 3β+2α lidar inversion. Improved constraints are needed due to the under-determination of the ill-posed problem, and particularly are critical for the range of m_r and maximum value of the imaginary refractive index allowed in the inversions. Our simulations have indicated that given a refractive index for simulating optical data of $m_{truth} = m_{r,truth} + im_{i,truth}$, the retrievals are improved when the permitted m_r is within $\pm 0.1 m_{r,truth}$ and maximum m_i is $2.5m_{i,truth}$. The analyses of AERONET retrievals for stations widely affected by pollution and biomass-burning particles (typically fine mode predominance and spherical particles) suggested dependency between m_r and m_i. The use of these dependences between m_r and m_i serves to delimit the range of m_r in the inversion if an estimation of m_i is known. The correlation between m_r and m_i obtained from AERONET database is consistent with the aerosol module of the Goddard Chemistry, Aerosol, Radiation, and Transport (GOCART) model. This relationship has allowed the definition of optimized constraints: When fine mode predominates, the optimized constraints set r_{max} = 2μm and any value for m_i is possible because fine particles in GOCART. For a mixture of fine and coarse modes the optimized inversion assumes different mixtures of the species assumed in GOCART which has suggested m_i be typically below 0.04 and highly variable in value. However, constraints in the range of inversions have not been possible and the optimized constraints sets r_{max} = 10 μm. The optimized inversion has assumed that cases of only coarse mode predominance are assumed as a particular case of mixture with fine mode negligible. Dust particles are excluded in our study as we are dealing only with spherical particles. Retrievals of aerosol microphysical properties for non-spherical particles require further analyses that were beyond the scope of this work.

The optimization of the stand stand-alone $3\beta+2\alpha$ lidar inversion transfers AERONET/GOCART assumptions to the lidar inversion, and therefore any uncertainties in AERONET/GOCART are carried along too. Nevertheless, the approach of optimized constraints is a reasonable tradeoff since AERONET retrievals possess much higher information content with respect to column-effective aerosol properties and the use of the GOCART model constrains the possible aerosol types. Future improvements in AERONET retrievals or in

GOCART model refinement can be transferred to this optimized constraint technique in the future as well.

The computation of the optimized constraints from 3β+2α measurements is possible through the analyses of the Angstrom exponent of extinction (γ_α) and spectral extinction-to-backscattering lidar ratios (LR) using a-priori information derived from GOCART. Although no additional measurements are required, the use of optimized constraints has revealed a better optimization of the stand-alone 3β+2α lidar inversion. Actually, such optimization allows retrievals of complex refractive index within the uncertainties claimed in the bibliography and even reduces these uncertainties in m_i to ±50%. Optimized constraints are also critical for the retrievals of single scattering albedo (SSA). However, limitations have been found and when fine mode predominates SSA retrievals are only feasible at 355 and 532 nm, while as the coarse mode contribution increases SSA retrievals at 1064 become feasible. But we comment that the use of optimized constraints implies that aerosol properties follow the relationship in refractive index indicated from the AERONET retrievals and when aerosol size follows the representation of bimodal size distribution indicated in GOCART. Also, we recall that the under-determination of the 3β+2α ill-posed problem does not allow retrieval of the spectral dependence of m_i and, therefore the methodology proposed provides an effective size distribution with the same refractive index for both modes.

The Deriving Information on Surface Conditions from COlumn and VERtically Resolved Observations Relevant to Air Quality (DISCOVER-AQ) field campaigns held in Texas (2013), California (2014) and Colorado (2014) have provided a unique dataset for the evaluation of the SSA retrievals using stand-alone 3β+2α lidar inversion with optimized constraints. Airborne HSRL-2 and in-situ measurements were provided by NASA Langley Research Center providing more than 1500 correlative spirals under different aerosol conditions. The optimized constraints were compared with the aerosol typing algorithm using aerosol depolarization measurements (δ), and generally very good agreement was found. The evaluation of SSA using in-situ measurements as reference at the wavelength of 532 nm have revealed very good agreement between both techniques with the differences being within the standard deviations associated with each technology. Actually, mean differences were nearly zero, while standard deviations were approximately 0.02 when $m_i < 0.01$ and 0.04 when $m_i > 0.01$. Limitations were found for cases of mixture of particles and $m_i < 0.01$ which have been explained by the presence of coarse particles which SSA retrievals are only feasible at 1064 nm. Overall, the stand-alone $3\beta+2\alpha$ lidar inversion with constraints has been demonstrated as a powerful tool to provide SSA retrievals with high temporal resolution in spite of technique limitations.

To date it has not been possible to integrate linear depolarization (δ) measurements into the microphysical inversion. Nonetheless such measurements by HSRL-2 system during DISCOVER-AQ have been essential for evaluating the optimized constraints. Very good agreement between the aerosol typing algorithm using aerosol intensive parameters and the optimized constraints has been observed. Further work is being carried out in using depolarization to separate dust (no spherical particles) from the rest of the aerosol particles that are assumed as spherical, and therefore to study the real capabilities of the stand-alone lidar inversion for retrieving dust microphysical properties and SSA. Evaluations of SSA provided by global models versus HSRL-2 retrievals are being done for NASA field campaigns such as DISCOVER-AQ and ORACLES.

Acknowledgments

This work was supported by the Marie Skłodowska-Curie Research Innovation and Staff Exchange (RISE) GRASP-ACE (grant agreement No 778349), and by the NASA Atmospheric Composition Program and by the NASA Aerosols, Clouds, Ecosystems mission. The authors thankfully acknowledge the AERONET team for maintaining the stations used in this work and to the NOAA Air Research Laboratory for providing the HYSPLIT model.We specially knowledge Dra. Sharon Burton, Dr. Richard A. Ferrare and the rest of the NASA Langley HSRL-2 for their comments to improve the manuscript. We finally express our gratitude to the LARGE team at NASA Langle for providing data from P3B airplane.

References

Alados-Arboledas, L., Müller, D., Guerrero-Rascado, J.L., Navas-Guzmán, F., Pérez-Ramírez, D., Olmo, F.J. (2011) Optical and microphysical properties of fresh biomass burning aerosol retrieved by Raman lidar, and star-and sun-photometry. *Geophysical Research Letters* 38.

Alexandrov, M.D., Mishchenko, M.I. (2017) Information content of bistatic lidar observations of aerosols from space. *Optics Express* 25, A134-A150.

Allen, R.J., Sherwood, S.C. (2010) Aerosol-cloud semi-direct effect and land-sea temperature contrast in a GCM. *Geophysical Research Letters 37*, L07702.

Anderson, T.L., Ogren, J.A. (1998) Determining Aerosol Radiative Properties Using the TSI 3563 Integrating Nephelometer. *Aerosol Science and Technology*, 29, 57-69.

Andrews, E. (2004) In situ aerosol profiles over the Southern Great Plains cloud and radiation test bed site: 1. Aerosol optical properties. *Journal of Geophysical Research*, 109.

Baars, H., Ansmann, A., Althausen, D., Engelmann, R., Heese, B., Müller, D., Artaxo, P., Paixao, M., Pauliquevis, T., Souza, R. (2012) Aerosol profiling with lidar in the Amazon Basin during the wet and dry season*. Journal of Geophysical Research: Atmospheres*, 117, D21201.

Bockman, C., Miranova, I., Muller, D., Schneidenbach, L., Nessler, R. (2005) Microphysical aerosol parameters from multiwavelength lidar. *J. Opt. Soc. Am. A.* 22, 518-528.

Boucher, O., Randall, D., Artaxo, P., Bretherton, C., Feingold, G., Foster, P., Kerminen, V.-M., Kondo, Y., Liao, H., Lohmann, U., Rasch, P., Satheesh, S.K., Sherwood, S., Stevens, B., Zhang, X.Y., (2013) Clouds and Aerosols, in: Stocker, T.F., Qin, D., Plattner, G.-K., Tignor, M., Allen, S.K., Boschung, J., Nauels, A., Xia, Y., Bex, V., Midgley, P.M. (Eds.), Climate Change 2013: The Physical Science Basis. Contribution of Working Group I to the Fifth Assessment Report of the Intergovernmental Panel on Climate Change. Cambridge University Press, Cambridge, United Kingdon and New York, NY, USA, pp. 571-657.

Buchard, V., da Silva, A.M., Colarco, P.R., Darmenov, A., Randles, C.A., Govindaraju, R., Torres, O., Campbell, J., Spurr, R. (2015) Using the OMI aerosol index and absorption aerosol optical depth to evaluate the NASA MERRA Aerosol Reanalysis. *Atmospheric Chemistry and Physics*, 15, 5743-5760.

Burton, S.P., Ferrare, R.A., Hostetler, C.A., Hair, J.W., Rogeres, R.R., Obland, M.D., Obland, M.D., Butler, C.F., Cook, A.L., Harper, D.B., and Froyd., K.D. (2012) Aerosol classification using airborne High Spectral Resolution Lidar measurements - methodology and examples. *Atmospheric Measurement Techniques,* 5, 73-98.

Burton, S.P., Ferrare, R.A., Vaughan, M.A., Omar, A.H., Rogers, R.R., Hostetler, C., and Hair, J.W. (2013) Aerosol classification from airborne HSRL and comparisons with the CALIPSO vertical feature mask. *Atmospheric Measurement Techniques*, 6, 1397-1412.

Burton, S.P., Vaughan, M.A., Ferrare, R.A., Hostetler, C.A. (2014) Separating mixtures of aerosol types in airborne High Spectral Resolution Lidar data. *Atmospheric Measurement Techniques*, 7, 419-436.

Burton, S.P., Hair, J.W., Kahnert, M., Ferrare, R.A., Hostetler, C.A., Cook, A.L., Harper, D.B., Berkoff, T.A., Seaman, S.T., Collins, J.E., Fenn, M.A., and Rogers, R.R. (2015) Observations of the spectral dependence of linear particle depolarization ratio of aerosols using NASA Langley airborne High Spectral Resolution Lidar. *Atmospheric Chemistry and Physics*, 15, 13453-13473.

Burton, S.P., Chemyakin, E., Liu, X., Knobelspiesse, K., Stamnes, S., Sawamura, P., Moore, R.H., Hostetler, C.A., Ferrare, R.A. (2016) Information content and sensitivity of the $3\beta+2\alpha$lidar measurement system for aerosol microphysical retrievals. *Atmospheric Measurement Techniques*, 9, 5555-5574.

Burton, S. P., Hostetler, C. A., Cook, A. L., Hair, J. W., Seaman, S. T., Scola, S., Harper, D. B., Smith, J. A., Fenn, M. A., Ferrare, R. A., Saide, P. E., Chemyakin, E. V., and Müller, D.: Calibration of a high spectral resolution lidar using a Michelson interferometer, with data examples from ORACLES, *Applied Optics*, 57, 6061-6075, 2018.

Chin, M., Rood, R.B., Lin, S.-J., Müller, J.-F., Thompson, A.M. (2000) Atmospheric sulfur cycle simulated in the global model GOCART: Model description and global properties. *Journal of Geophysical Research,* 105, 24671.

Chin, M., Ginoux, P., Kinne, S., Torres, O., Holben, B.N., Duncan, B.N., Martin, R.V., Logan, J.A., Higurashi, A., Nakajima, T. (2002) Tropospheric aerosol optical thickness from the GOCART model and comparisons with satellite and sun photometer measurements. *Journal of the Atmospheric Sciences*, 59, 461-483.

Chin, M., Chu, A., Levy, R., Remer, L., Kaufman, Y., Holben, B., Eck, T., Ginoux, P., Gao, Q. (2004) Aerosol distribution in the Northern Hemisphere during ACE-Asia: Results from global model, satellite observations, and Sun photometer measurements. *Journal of Geophysical Research: Atmospheres*, 109.

Clarke, A.D., Howell, S., Quinn, P.K., Bates, T.S., Ogren, J.A., Andrews, E., Jefferson, A., Massling, A., Mayol-Bracero, O., Maring, H., Savoie, D., Cass, G. (2002) INDOEX aerosol: A comparison and summary of chemical, microphysical, and optical properties observed from land, ship, and aircraft. *Journal of Geophysical Research*, 107, 8033.

Colarco, P.R., Gasso, S., Ahn, C., Buchard, V., da Silva, A.M. and Torres, O. (2017) Simulation of the Ozone Monitoring Instrument Aerosol Index using the NASA Goddard Earth Observing System Aerosol Reanalysis Products, *Atmospheric Measurement Techniques*, 10, 4121-4134.

Dubovik, O., Herman, M., Holdak, A., Lapyonok, T., Tanré, D., Deuzé, J.L., Ducos, F., Sinyuk, A., Lopatin, A. (2011) Statistically optimized inversion algorithm for enhanced retrieval of aerosol properties from spectral multi-angle polarimetric satellite observations. *Atmospheric Measurement Techniques,* 4, 975-1018.

Dubovik, O., Holben, B., Eck, T.F., Smirnov, A., Kaufman, Y.J., King, M.D., Tanre, D., Slutsker, I. (2002) Variability of absorption and optical properties of key aerosol types observed in worldwide locations. *Journal of the Atmospheric Sciences,* 59, 590-608.

Dubovik, O., King, M.D. (2000) A flexible inversion algorithm for retrieval of aerosol optical properties from Sun and sky radiance measurements. *Journal of Geophysical Research*, 105, 20673-20696.

Dubovik, O., Smirnov, A., Holben, B.N., King, M.D., Kaufman, Y., Eck, T.F., and Slutsker, I. (2000) Accuracy assesments of aerosol optical properties retrieved from Aerosol Robotic Network (AERONET) Sun and sky radiance measurements, *Journal of Geophysical Research*, 105, 9791-9806.

Dubovik, O., Sinyuk, A., Lapyonok, T., Holben, B.N., Mishchenko, M., Yang, P., Eck, T.F., Volten, H., Muñoz, O., Veihelmann, B., van der Zande, W.J., Leon, J.-F., Sorokin, M., Slutsker, I. (2006) Application of spheroid models to account for aerosol particle nonsphericity in remote sensing of desert dust. *Journal of Geophysical Research*, 111, D11208.

Eck, T.F., Holben, B.N., Ward, D.E., Mukelabai, M.M., Dubovik, O., Smirnov, A., Schafer, J.S., Hsu, N.C., Piketh, S.J., Queface, A., Le Roux, J., Swap, R.J., Slutsker, I. (2003) Variability of biomass burning aerosol optical characteristics in southern Africa during the SAFARI 2000 dry season campaign and a comparison of single scattering albedo estimates from radiometric measurements. *Journal of Geophysical Research,* 108.

Eck, T.F., Holben, B.N., Sinyuk, A., Pinker, R.T., Goloub, P., Chen, H., Chatenet, B., Li, Z., Singh, R.P., Tripathi, S.N., Reid, J.S., Giles, D.M., Dubovik, O., O´Neill, N.T., Smirnov, A., Wang, P., and Xia, X. (2010) Climatological aspects of the optical properties of fine/coarse mode aerosol mixtures*. Journal of Geophysical Research,* 115, D19205.

Feingold, G. (2005) On smoke suppression of clouds in Amazonia. *Geophysical Research Letters,* 32, L02804.

Fernald, F.G. (1984) Analysis of atmospheric lidar observations: some comments. *Applied Optics,* 23, 652-653.

Ghan, S.J., Liu, X., Easter, R.C., Zaveri, R., Rasch, P.J., Yoon, J.H., Eaton, B. (2012) Toward a Minimal Representation of Aerosols in Climate Models: Comparative Decomposition of Aerosol Direct, Semidirect, and Indirect Radiative Forcing. *Journal of Climate*, 25, 6461-6476.

Ginoux, P., Chin, M., Tegen, I., Prospero, J.M., Holben, B., Dubovik, O., Lin, S.-J. (2001) Sources and distributions of dust aerosols simulated with the GOCART model. *Journal of Geophysical Research,* 106, 20255.

Hair, J.W., Hostetler, C.A., Cook, A.L., Harper, D.B., Ferrare, R.A., Mack, T.L., Welch, W., Ramos-Izquierdo, L., Hovis, F. (2008) Airborne High Spectral Resolution Lidar for profiling aerosol optical properties. *Applied Optics*, 47, 6734-6753.

Holben, B.N., Eck, T.F., Slutsker, I., Tanre, D., Buis, J.P., Setzer, A., Vermote, E., Reagan, J.A., Kaufman, Y.J., Nakajima, T., Lavenu, F., Jankowiak, I., Smirnov, A. (1998) AERONET- A federated instrument network and data archive for aerosol characterization. *Remote Sensing of Environment,* 66, 1-16.

Holben, B.N., Eck, T.F., Slutsker, I., Smirnov, A., Sinyuk, A., Schafer, J., Giles, D., and Dubovik, O. (2006) AERONET's Version 2.0 quality assurance criteria. *Proc. SPIE* Vol. 6408, 6408Q.

Illingworth, A.J., Barker, H.W., Beljaars, A., Ceccaldi, M., Chepfer, H., Clerbaux, N., Cole, J., Delanoë, J., Domenech, C., Donovan, D.P., Fukuda, S., Hirakata, M., Hogan, R.J., Huenerbein, A., Kollias, P., Kubota, T., Nakajima, T., Nakajima, T.Y., Nishizawa, T., Ohno, Y., Okamoto, H., Oki, R., Sato, K., Satoh, M., Shephard, M.W., Velázquez-Blázquez, A., Wandinger, U., Wehr, T., van Zadelhoff, G.J. (2015) The EarthCARE Satellite: The Next Step Forward in Global Measurements of Clouds, Aerosols, Precipitation, and Radiation. *Bulletin of the American Meteorological Society*, 96, 1311-1332.

Koren, I., Kaufman, Y.J., Remer, L. A., Martins, J.V. (2004) Measurement of the effect of Amazon smoke on inhibition of cloud formation. *Science,* 1342-1345.

Klett, J.D. (1981) Stable analytical inversion solution for processing lidar returns. *Applied Optics,* 20, 211-220.

Klett, J.D. (1985) Lidar inversion with variable backscatter/extinction ratios. *Applied Optics* 24.

Koch, D., Del Genio, A.D. (2010) Black carbon semi-direct effects on cloud cover: review and synthesis. *Atmospheric Chemistry and Physics,* 10, 7685-7696.

Loeb, N.G., Su, W. (2010) Direct Aerosol Radiative Forcing Uncertainty Based on a Radiative Perturbation Analysis. *Journal of Climate,* 23, 5288-5293.

McComiskey, A., Schwartz, S.E., Schmid, B., Guan, H., Lewis, E.R., Ricchiazzi, P., Ogren, J.A. (2008) Direct aerosol forcing: Calculation from observables and sensitivities to inputs. *Journal of Geophysical Research*, 113.

McNaughton, C.S., Clarke, A.D., Howell, S.G., Pinkerton, M., Anderson, B., Thornhill, L., Hudgins, C., Winstead, E., Dibb, J.E., Scheuer, E., Maring, H. (2007) Results from the DC-8 Inlet Characterization Experiment (DICE): Airborne Versus Surface Sampling of Mineral Dust and Sea Salt Aerosols. *Aerosol Science and Technology,* 41, 136-159.

Mishchenko, M.I., Alexandrov, M.D., Cairns, B., Travis, L.D. (2016) Multistatic aerosol–cloud lidar in space: A theoretical perspective. *Journal of Quantitative Spectroscopy and Radiative Transfer*, 184, 180-192.

Müller, D., Wandinger, U., and Ansmann, A. (1999a) Microphysical particle parameters from extinction and backscatter lidar data by inversion with regularization: theory, *Applied Optics,* 38, 2346-2368.

Müller, D., Wandinger, U., and Ansmann, A. (1999b) Microphysical particle parameters from extinction and backscatter lidar data by inversion with regularization: simulation, *Applied Optics*, 38, 2358-2357.

Müller, D., Kolgotin, A., Mattis, I., Petzold, A., Stohl, A. (2011) Vertical profiles of microphysical particle properties derived from inversion with two-dimensional regularization of multiwavelength Raman lidar data: experiment. *Applied Optics,* 50, 2069-2079.

Müller, D., Mattis, I., Ansmann, A., Wehner, B., Althausen, D., Wandinger, U., Dubovik, O. (2004) Closure study on optical and microphysical properties of a mixed urban and Arctic haze air mass observed with Raman lidar and Sun photometer. *Journal of Geophysical Research*, 109.

Müller, D., Mattis, I., Wandinger, U., Ansmann, A., Althausen, D. (2005) Raman lidar observations of aged Siberian and Canadian forest fire smoke in the free troposphere over Germany in 2003: Microphysical particle characterization. *Journal of Geophysical Research*, 110.

Müller, D., Böckmann, C., Kolgotin, A., Schneidenbach, L., Chemyakin, E., Rosemann, J., Znak, P., and Romanov, A. (2016) Microphysical particle properties derived from inversion algorithms developed in the framework of EARLINET. *Atmospheric Measurement Techniques*, 9, 5007-5035

Navas-Guzmán, F., Müller, D., Bravo-Aranda, J.A., Guerrero-Rascado, J.L., Granados-Muñoz, M.J., Pérez-Ramírez, D., Olmo, F.J., Alados-Arboledas, L. (2013) Eruption of the

Eyjafjallajökull Volcano in spring 2010: Multiwavelength Raman lidar measurements of sulphate particles in the lower troposphere. *Journal of Geophysical Research: Atmospheres,* 118, 1804-1813.

Mie, G. (1908) BeiträgezurOptiktrüberMedien, speziellkolloidalerMetallösungen, *Ann. Phys.*-Berlin, 25, 377–445.

Noh, Y.M., Müller, D., Shin, D.H., Lee, H., Jung, J.S., Lee, K.H., Cribb, M., Li, Z., Kim, Y.J. (2009) Optical and microphysical properties of severe haze and smoke aerosol measured by integrated remote sensing techniques in Gwangju, Korea. *Atmospheric Environment,* 43, 879-888.

Norman, M.L., Qian, J., Miller, R.E., Worsnop, D.R. (1999) Infrared complex refractive indices of supercooled liquid HNO_3/H_2O aerosols, *Journal of Geophysical Research,* 104, 30571-30584.

Pappalardo, G., Amodeo, A., Apituley, A., Comeron, A., Freudenthaler, V., Linné, H., Ansmann, A., Bösenberg, J., D'Amico, G., Mattis, I., Mona, L., Wandinger, U., Amiridis, V., Alados-Arboledas, L., Nicolae, D., and Wiegner, M. (2014) EARLINET: towards an advanced sustainable European aerosol lidar network, *Atmospheric Measurement Techniques,* 7, 2389-2409.

Pérez-Ramírez, D., Veselovskii, I., Whiteman, D.N., Suvorina, A., Korenskiy, M., Kolgotin, A., Holben, B., Dubovik, O., Siniuk, A., Alados-Arboledas, L. (2015) High temporal resolution estimates of columnar aerosol microphysical parameters from spectrum of aerosol optical depth by linear estimation: application to long-term AERONET and star-photometry measurements. *Atmospheric Measurement Techniques,* 8, 3117-3133.

Pérez-Ramírez, D., Whiteman, D.N., Veselovskii, I., Kolgotin, A., Korenskiy, M., Alados-Arboledas, L. (2013) Effects of systematic and random errors on the retrieval of particle microphysical properties from multiwavelengthlidar measurements using inversion with regularization. *Atmospheric Measurement Techniques,* 6, 3039-3054.

Pérez-Ramírez, D., Andrade, M., Eck, T.F., Stein, A., O'Neill, N.T., Lyamani, H., Gassó, S., Whiteman, D.N., Veselovskii, I., Velarde, F., and Alados-Arboledas, L. (2017) Multi yearaerosol characterization in the tropical Andes in adjacent Amazonia using AERONET measurements. *Atmospheric Environment*, 166, 412-432.

Persad, G.G., Ming, Y., Ramaswamy, V. (2012) Tropical Tropospheric-Only Responses to Absorbing Aerosols. *Journal of Climate*, 25, 2471-2480.

Pilat, J., Charlson, R.J. (1966) Theoretical and optical studies of humidity effects on the size distribution of a hygroscopic aerosol. J. Rech. Atmos., 165-170.

Reid, J., Kuehn, R.E., Holz, R.E., Eloranta, E.W., Kaku, K.C., Kuang, S., Newchurch, M.J., Thopson, A.M., Trepte, C.R., Zhang, J., Atwood, S.A., Hand, J.L., Holben, B.N., Minnis, P., and Posselt, D.J. (2017) Ground-based High Spectral Resolution Lidar observation of aerosol vertical distribution in the summertime Southeast United States, *Journal of Geophysical Research: Atmospheres*, 112, 2970-3004.

Richwine, L. J., Clapp, M.L., Miller, R.E., and Worsnop, D.R. (1995) Complex refractive indices in the infrared of nitric acid trihydrate aerosols, *Geophysical Research Letters*, 22, 2625-2628.

Rogers, R.R., Hair, J.W., Hostetler, C.A., Ferrare, R.A., Obland, M.D., Cook, A.L., Harper, D.B., Burton, S.P., Shinozuka, Y., McNaughton, C.S., Clarke, A.D., Redemann, J., Russel, P.B., Livingston, J.M., Kleinman, L.I. (2009) NASA LaRC airborne high spectral resolution lidar aerosol measurements during MILAGRO: observations and validation. *Atmospheric Chemistry and Physics*, 9.

Sakaeda, N., Wood, R., Rasch, P.J. (2011) Direct and semidirect aerosol effects of southern African biomass burning aerosol. *Journal of Geophysical Research,* 116.

Sawamura, P., Müller, D., Hoff, R.M., Hostetler, C.A., Ferrare, R.A., Hair, J.W., Rogers, R.R., Anderson, B.E., Ziemba, L.D., Beyersdorf, A.J., Thornhill, K.L., Winstead, E.L., Holben, B.N. (2014) Aerosol optical and microphysical retrievals from a hybrid multiwavelengthlidar data set – DISCOVER-AQ 2011. *Atmospheric Measurement Techniques,* 7, 3095-3112.

Sawamura, P., Moore, R.H., Burton, S. P., Chemyakin, E., Müller, D., Kolgotin, A., Ferrare, R.A., Hostetler, C.A., Ziemba, L.D., Beyersdorf, A.J., and Anderson, B.E. (2017) HSRL-2 aerosol optical measurements and microphysical retrievals vs. airborne in situ measurements during DISCOVER-AQ 2013: an intercomparison study. *Atmospheric Chemistry and Physics,* 17, 7229-7243.

Schuster, G.L., Dubovik, O., Arola, A. (2016a) Remote sensing of soot carbon – Part 1: Distinguishing different absorbing aerosol species. *Atmospheric Chemistry and Physics,* 16, 1565-1585.

Schuster, G.L., Dubovik, O., Arola, A., Eck, T.F., Holben, B.N. (2016b) Remote sensing of soot carbon – Part 2: Understanding the absorption Ångström exponent. *Atmospheric Chemistry and Physics,* 16, 1587-1602.

Shipley, S.T., Tracy, D.H., Eloranta, E.W., Trauger, J.T., Sroga, J.T., Roesler, F.L., Weinman, J.A. (1983) High spectral resolution lidar to measure optical scattering properties of atmospheric aerosols. 1: Theory and instrumentation. *Applied Optics,* 22, 3716-3724.

Stein, A.F., Draxler, R.R., Rolph, G.D., Stunder, B.J.B., Cohen, M.D., Ngan, F. (2015) NOAA's HYSPLIT Atmospheric Transport and Dispersion Modeling System. *Bulletin of the American Meteorological Society,* 96, 2059-2077.

Stier, P., Schutgens, N.A.J., Bellouin, N., Bian, H., Boucher, O., Chin, M., Ghan, S., Huneeus, N., Kinne, S., Lin, G., Ma, X., Myhre, G., Penner, J.E., Randles, C.A., Samset, B., Schulz, M., Takemura, T., Yu, F., Yu, H., Zhou, C. (2013) Host model uncertainties in aerosol radiative forcing estimates: results from the AeroCom Prescribed intercomparison study. *Atmospheric Chemistry and Physics*, 13, 3245-3270.

Stier, P., Seinfeld, J.H., Kinne, S., Boucher, H. (2007) Aerosol absorption and radiative forcing. *Atmospheric Chemistry and Physics*, 7, 5237-5261.

Tang, I, N. (1996) Chemical and size effects of hygroscopic aerosols on light scattering coefficients, *Journal of Geophysical Research*, 101, 19245-19250.

Tanré, D., Bréon, F.M., Deuzé, J.L., Dubovik, O., Ducos, F., François, P., Goloub, P., Herman, M., Lifermann, A., Waquet, F. (2011) Remote sensing of aerosols by using polarized, directional and spectral measurements within the A-Train: the PARASOL mission. *Atmospheric Measurement Techniques,* 4, 1383-1395.

Toon, O.B., Tolbert, M.A., Koehler, B.G., Middlebrook, A.M., and Jordan, J. (1994) Infrared optical constants of H20 ice, amorphous nitric acid solutions, and nitric acid hydrates, Journal of Geophysical Research, 99, 25631-25654.

Torres, O., Tanskanen, A., Veihelmann, B., Ahn, C., Braak, R., Bhartia, P.K., Veefkind, P., Levelt, P. (2007) Aerosols and surface UV products from Ozone Monitoring Instrument observations: An overview. *Journal of Geophysical Research,* 112.

Veselovskii, I., Dubovik, O., Kolgotin, A., Korenskiy, M., Whiteman, D.N., Allakhverdiev, K., Huseyinoglu, F. (2012) Linear estimation of particle bulk parameters from multi-wavelength lidar measurements*. Atmospheric Measurement Techniques*, 5, 1135-1145.

Volz, F.E.: (1973) Infrared optical constants of Ammonium Sulfate, Sahara dust, volcanic Pumice, and Flyash. Applied Optics, 12, 564-568.

Veselovskii, I., Dubovik, O., Kolgotin, A., Lapyonok, T., Di Girolamo, P., Summa, D., Whiteman, D.N., Mishchenko, M., Tanré, D. (2010) Application of randomly oriented spheroids for retrieval of dust particle parameters from multiwavelengthlidar measurements. *Journal of Geophysical Research,* 115.

Veselovskii, I., Kolgotin, A., Griaznov, V., Muller, D., Franke, K., Whiteman, D. (2004) Inversion of multiwavelength Raman lidar data for retrieval of bimodal aerosol size distribution. *Applied Optics,* 43.

Veselovskii, I., Kolgotin, A., Griaznov, V., Muller, D., Wandinger, U., Whiteman, D. (2002) Inversion with regularization for the retrieval of tropospheric aerosol parameters from multiwavelengthlidar sounding. *Applied Optics*, 41, 3685-3699.

Veselovskii, I., Kolgotin, A., Muller, D., Whiteman, D. (2005) Information content of multiwavelengthlidar data with respect to microphysical particle properties derived from eigenvalue analysis. *Applied Optics*, 44, 5292-5303.

Veselovskii, I., Whiteman, D.N., Kolgotin, A., Andrews, E., Korenskii, M. (2009) Demonstration of Aerosol Property Profiling by Multiwavelength Lidar under Varying Relative Humidity Conditions. *Journal of Atmospheric and Oceanic Technology,* 26, 1543-1557.

Veselovskii, I., Whiteman, D.N., Korenskiy, M., Kolgotin, A., Dubovik, O., Perez-Ramirez, D., Suvorina, A. (2013) Retrieval of spatio-temporal distributions of particle parameters from multiwavelengthlidar measurements using the linear estimation technique and comparison with AERONET*. Atmospheric Measurement Techniques,* 6, 2671-2682.

Veselovskii, I., Whiteman, D.N., Korenskiy, M., Suvorina, A., Kolgotin, A., Lyapustin, A., Wang, Y., Chin, M., Bian, H., Kucsera, T.L., Pérez-Ramírez, D., Holben, B. (2015) Characterization of forest fire smoke event near Washington, DC in summer 2013 with multi-wavelength lidar. *Atmospheric Chemistry and Physics*, 15, 1647-1660.

Virkkula, A. (2010) Correction of the Calibration of the 3-wavelength Particle Soot Absorption Photometer (3λ PSAP). *Aerosol Science and Technology* ,44, 706-712.

Wandinger, U., Muller, D., Bockman, C., Althausen, D., Matthias, V., Bosenberg, J., WeiB, V., Fiebig, M., Wendisch, M., Stohl, A., Ansmann, A. (2002) Optical and microphysical characterization of biomass- burning and industrial-pollution aerosols from multiwavelengthlidar and aircraft measurements. *Journal of Geophysical Research*, 107.

Wang, T., Li, S., Shen, Y., Deng, J., and Xie, M. (2010) Investigations on direct and indirect effect of nitrate on temperature and precipitation in China using a regional climate chemistry modeling system, Journal of Geophysical Research, 115, D00K26.

Welton, E., Campbell, J. (2002) Micropulse Lidar Signals: Uncertainty Analysis. *Journal of Atmospheric and Oceanic Technology*, 19, 2089-2094.

Wendisch, M., Hellmuth, O., Ansmann, A., Heintzenberg, J., Engelmann, R., Althausen, D., Eichler, H., Müller, D., Hu, M., Zhang, Y. (2008) Radiative and dynamic effects of absorbing aerosol particles over the Pearl River Delta, China. *Atmospheric Environment,* 42, 6405-6416.

Whiteman, D.N., Pérez-Ramírez, D., Veselovskii, I., Colarco, P., Buchard, V. (2018) Retrievals of aerosol microphysics from simulations of spaceborne multiwavelength lidar measurements *. Journal of Quantitative Spectroscopy & Radiative Transfer,* 205,27–39 .

Winker, D.M., Pelon, J., Coakley, J.A., Ackerman, S.A., Charlson, R.J., Colarco, P.R., Flamant, P., Fu, Q., Hoff, R.M., Kittaka, C., Kubar, T.L., Le Treut, H., McCormick, M.P., Mégie, G., Poole, L., Powell, K., Trepte, C., Vaughan, M.A., Wielicki, B.A. (2010) The CALIPSO Mission: A Global

3D View of Aerosols and Clouds. *Bulletin of the American Meteorological Society*, 91, 1211-1229.

Yorks, J.E., McGill, M.J., Palm, S.P., Hlavka, D.L., Selmer, P.A., Nowottnick, E.P., Vaughan, M.A., Rodier, S.D., Hart, W.D. (2016) An overview of the CATS level 1 processing algorithms and data products. *Geophysical Research Letters*, 43, 4632-4639.

Yoshimori, M., Broccoli, A.J. (2008) Equilibrium Response of an Atmosphere–Mixed Layer Ocean Model to Different Radiative Forcing Agents: Global and Zonal Mean Response. *Journal of Climate*, 21, 4399-4423.

Zarzycki, C.M., and Bond, T.C. (2010) How much can the vertical distribution of black carbon affect its global direct radiative forcing?, *Geophysical Research Letters,* 37, L20807.

Zhang, H., Shen, Z., Wei, X., Zhang, M., and Li, Z. (2012) Comparison of optical properties of nitrate and sulfate aerosol and the radiave forcing to nitrate in China, Atmospheric Research, 113, 113-125.

Ziemba, L.D., Lee Thornhill, K., Ferrare, R., Barrick, J., Beyersdorf, A.J., Chen, G., Crumeyrolle, S.N., Hair, J., Hostetler, C., Hudgins, C., Obland, M., Rogers, R., Scarino, A.J., Winstead, E.L., Anderson, B.E. (2013) Airborne observations of aerosol extinction by in situ and remote-sensing techniques: Evaluation of particle hygroscopicity. *Geophysical Research Letters*, 40, 417-422.

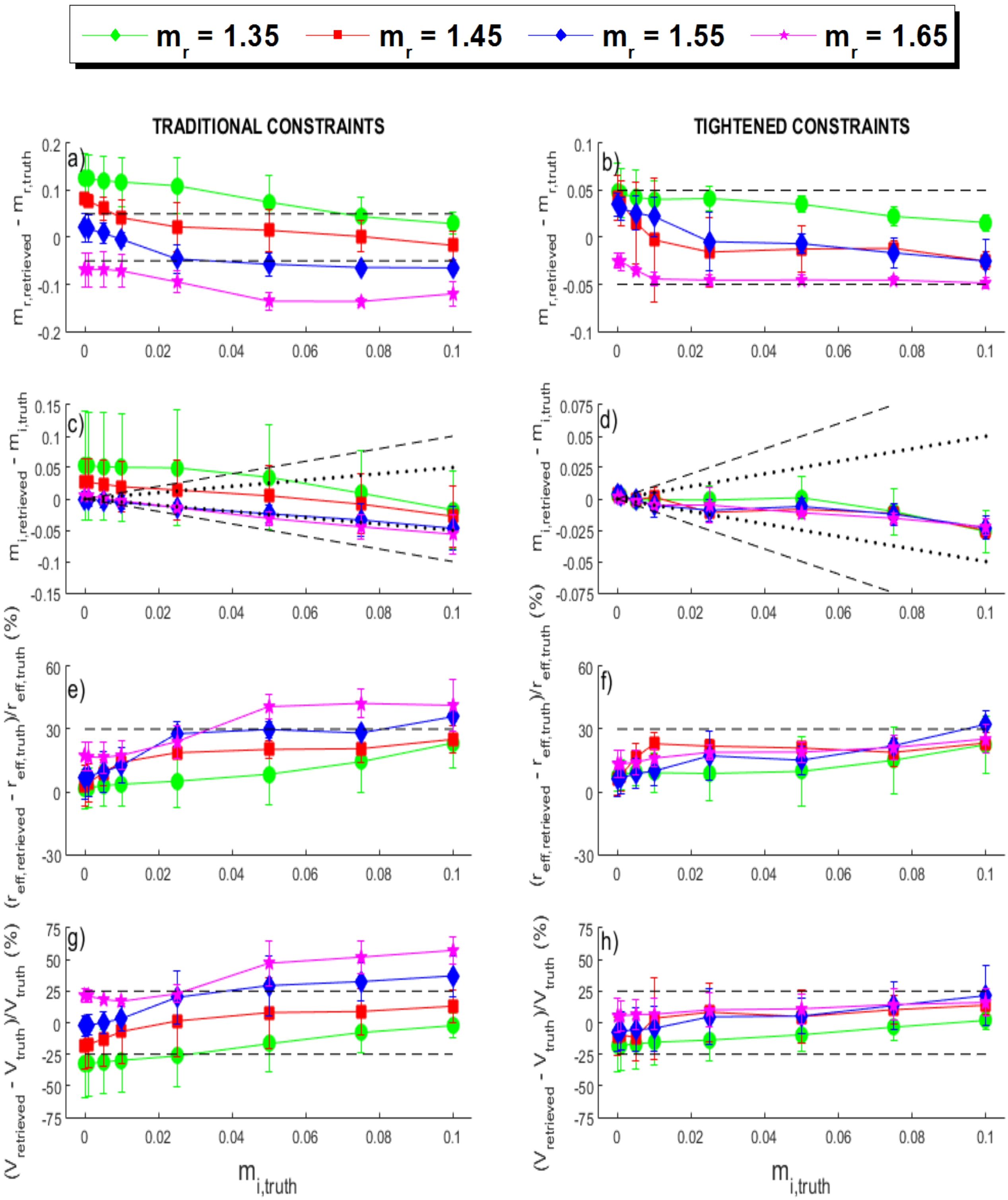

m_r = 1.35
m_r = 1.45
m_r = 1.55
m_r = 1.65
TRADITIONAL CONSTRAINTS
TIGHTENED CONSTRAINTS
a)
b)
c)
d)
e)
f)
g)
h)
m_r,retrieved - m_r,truth
m_i,retrieved - m_i,truth
(r_eff,retrieved - r_eff,truth)/r_eff,truth (%)
(V_retrieved - V_truth)/V_truth (%)
m_i,truth

<u>Figure 1:</u> Differences between retrieved and modeled aerosol parameters as a function of imaginary refractive index for inversions with no limit in the real refractive index and maximum imaginary refractive index of 0.1, and for inversions when tightened constraints are applied. Vertical lines are standard deviations because inversions are done for different sets of r_{fine}. (a) – (b) Differences between retrieved ($m_{r,retrieved}$) and modeled ($m_{r,model}$) real refractive index, (c) – (d) Differences between retrieved ($m_{i,retrieved}$) and modeled ($m_{i,model}$) imaginary refractive (e) – (f) Differences between retrieved ($R_{eff,retrieved}$) and modeled ($R_{eff,model}$) effective radius and (g)-(h) Differences between retrieved ($V_{retrieved}$) and modeled (V_{model}) volume concentration. Dashed black lines are the uncertainties reported in the bibliography for the retrievals of aerosol microphysical properties (dotted lines in the absolute differences in imaginary refractive index are for the assumption of reduced uncertainties in m_i to ±50%).

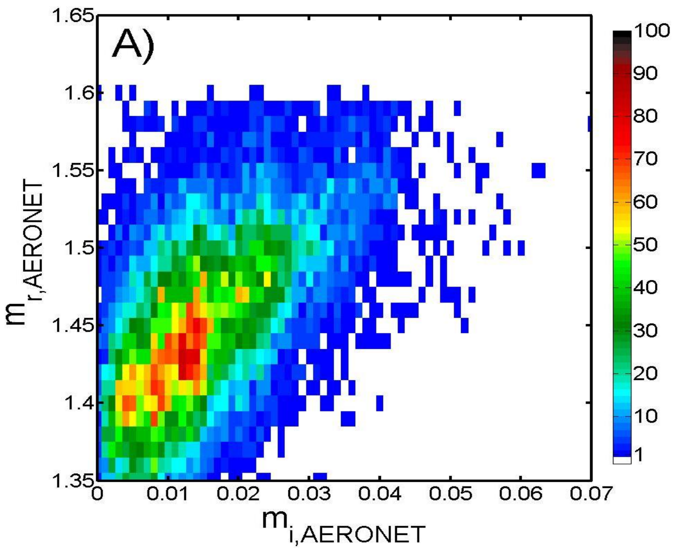

Figure 2: Color density plots of real refractive index as a function of the imaginary index. Data corresponds to all AERONET Level 2.0 retrievals described in Table 1, with a total number of 15392.

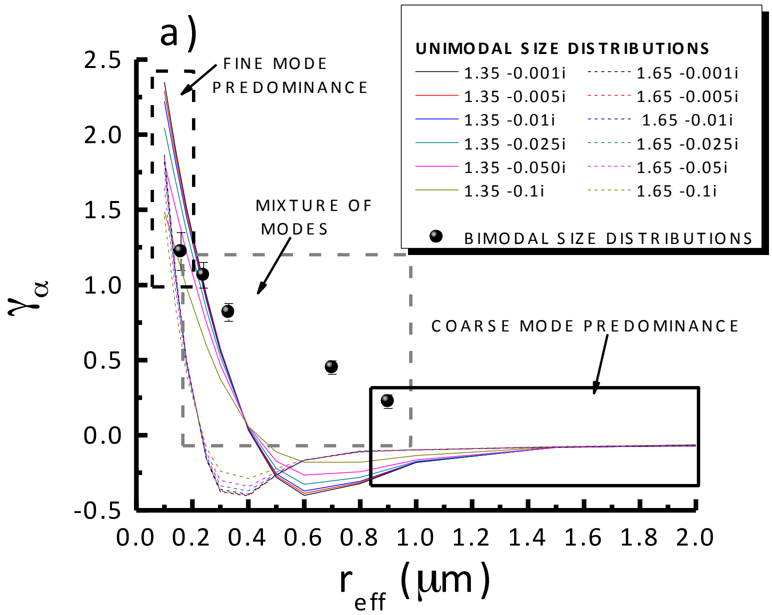

Figure 3: Extinction Angstrom exponent between 355 and 532 nm (γ_α(355-532)) versus the effective radius of selected size distributions. Computations are shown for unimodal size distributions with r_M = 0.10, 0.14, 0.18, 0.25, 0.3, 0.4, 0.5, 0.6, 0.8, 1.0, 1.5 and 2 μm with σ_M =0.4 μm. The values of the real part of the refractive index are 1.35, 1.45, 1.55 and 1.65 while the imaginary part is one of 0.001, 0.005, 0.01, 0.025, 0.05 and 0.1. Also, bimodal size distributions are used with the same set of refractive indexes.

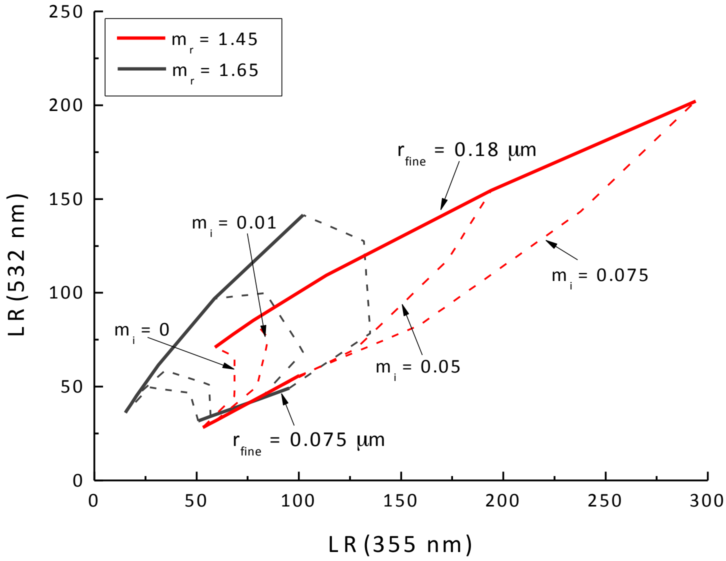

Figure 4: Spectral dependences of extinction-to-backscatterlidar ratios (LR) for different unimodal size distributions of different modal radius (r_{fine}) = 0.075, 0.10, 0.14 and 0.18 µ and imaginary refractive indexes (m_i) of 0.001, 0.005, 0.01, 0.025, 0.05 and 0.075. Continuous lines represent fixed r_{fine} and variable mi, while dashed lines imply fixed m_i and variable r_{fine}. Data are shown for m_r = 1.55 (red lines) and for m_r = 1.65 (black lines)

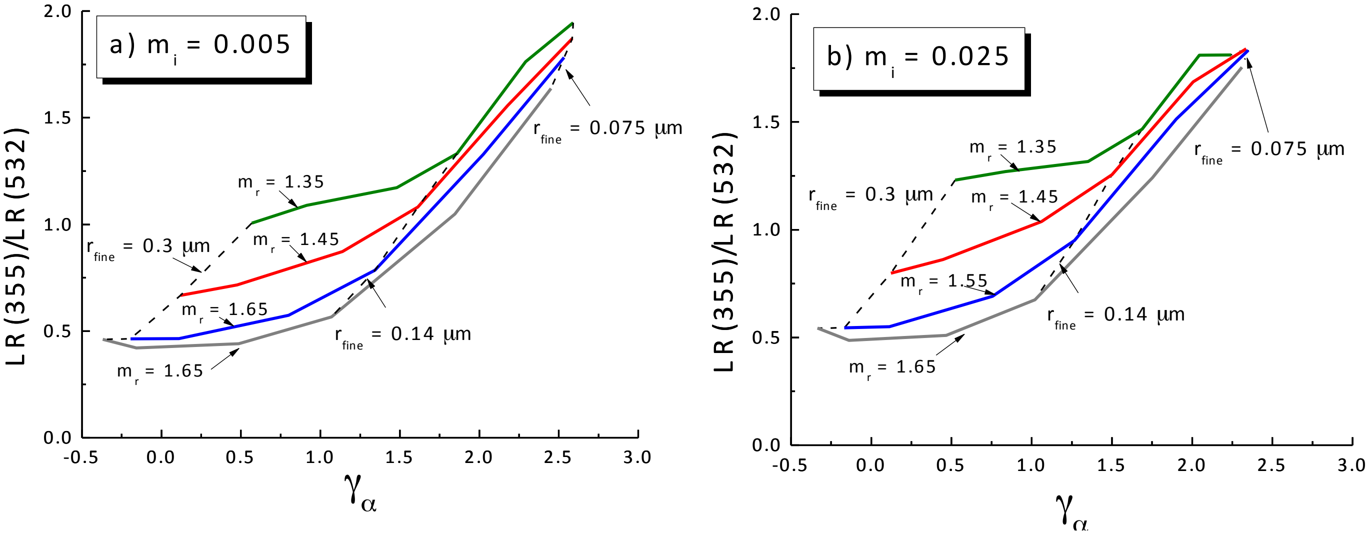

Figure 5: Ratio of the extinction-to-backscatter lidar ratios (LR(355)/LR(532)) as function of the Angstrom exponent of extinction (γ_α(355-532)) for different unimodal size distributions, r_M = 0.075, 0.10, 0.14, and 0.18 µm and m_r = 1.35, 1.45, 1.55 and 1.65. The width is fixed with σ_M =0.4 µm. Plots are shown for m_i = 0.005 and 0.025. Dashed lines represent size distributions with fixed r_M and variable m_r, while continuous color lines represent size distributions with fixed m_r and variable r_M.

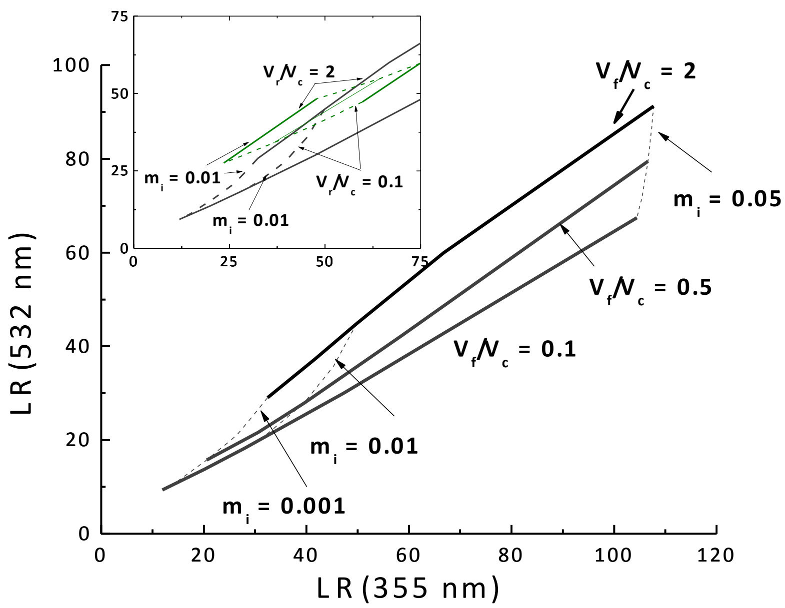

Figure 6: Spectral dependences of extinction-to-backscatter lidar ratios (LR) for different bimodal size distributions with different ratios between fine and coarse volumes (V_f/V_c) and imaginary refractive indexes (m_i) of 0.001, 0.005, 0.01, 0.02, 0.03 and 0.04. Data are shown for m_r = 1.55 (Black lines), and in the small square is also represented for m_r= 1.35. Dashed lines represent size distributions with fixed m_i and variable V_f/V_c, while continuous lines represent size distributions with fixed V_f/V_c and variable m_i.

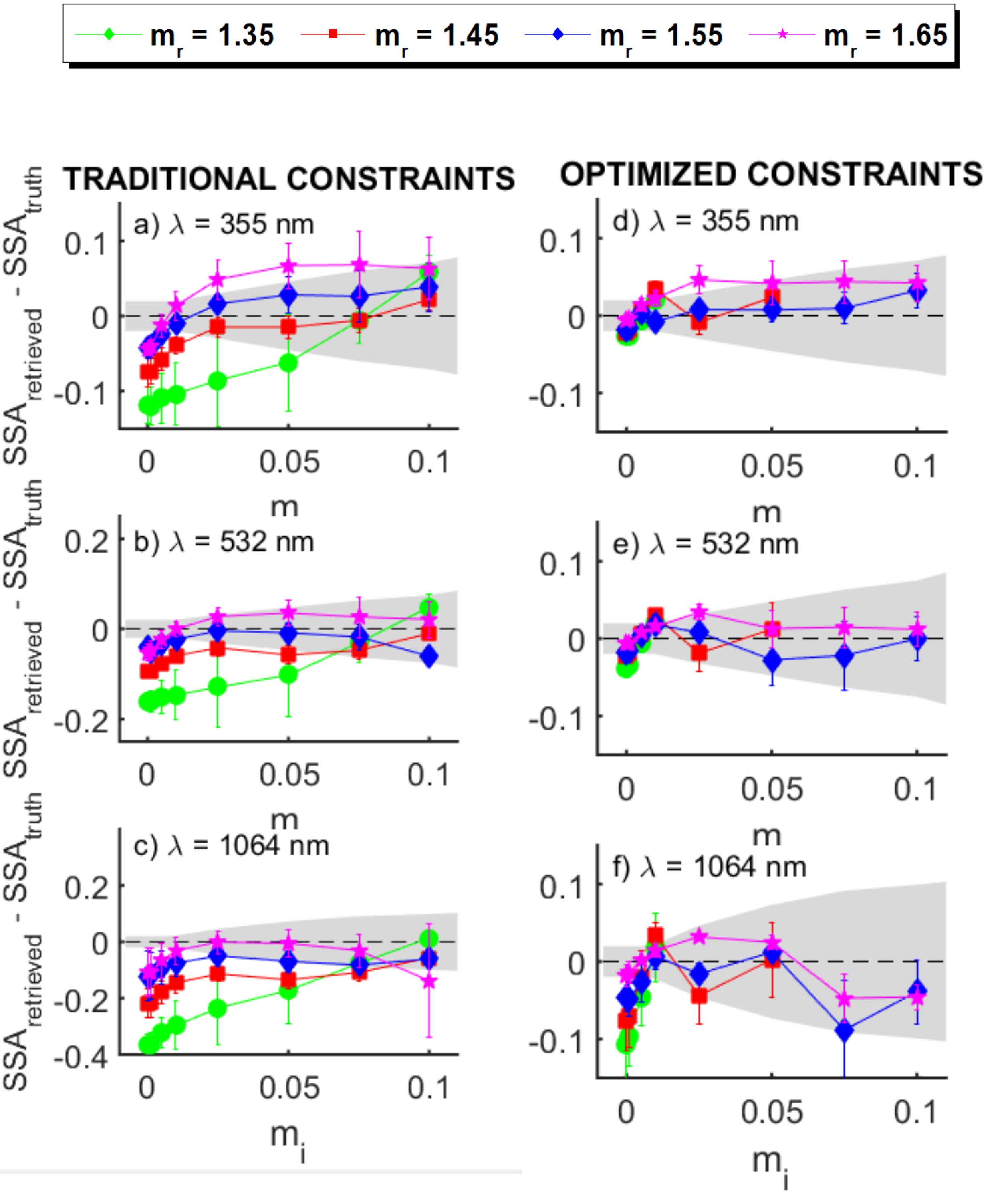

Figure 7: Differences between retrieved ($SSA_{retrieved}$) and truth (SSA_{truth}) single scattering albedo as a function of imaginary refractive index. The left panel presents the results when traditional constraints are applied in the stand-alone 3β+2α lidar inversion, while right panel is representative when the optimized constraints are applied

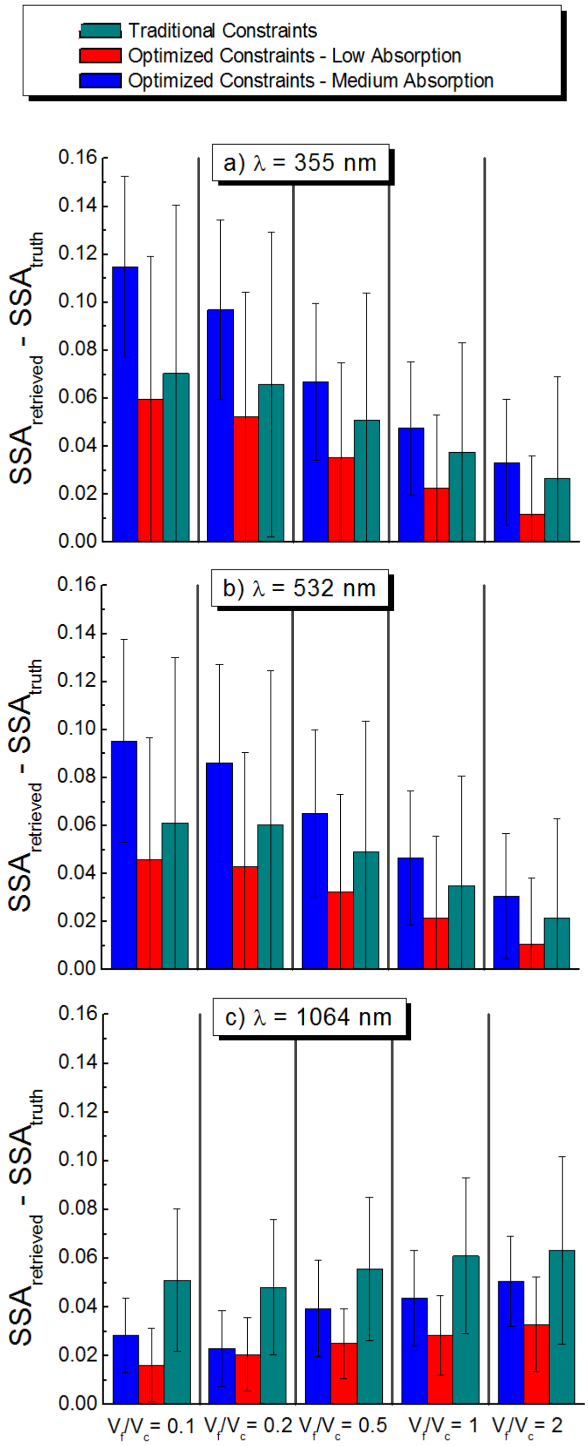

<u>Figure 8:</u> Absolute value of differences between retrieved and true values of aerosol single scattering albedo (SSA) as a function of the ratio between volumes of fine and coarse mode (V_f/V_c) for (a) λ = 355 nm (b) λ = 532 nm and (c) λ = 1064 nm. Results are shown for cases when traditional constraints are applied in the inversion ($m_{i,max}$ = 0.1 and no limitations in m_r) and for cases when optimized constraints are applied for limiting low ($m_i < 0.01$) and medium absorption ($m_i > 0.01$) cases. Vertical bars are the standard deviations of averaging the values of the different $m_{r,truth}$ and $m_{i,truth}$.

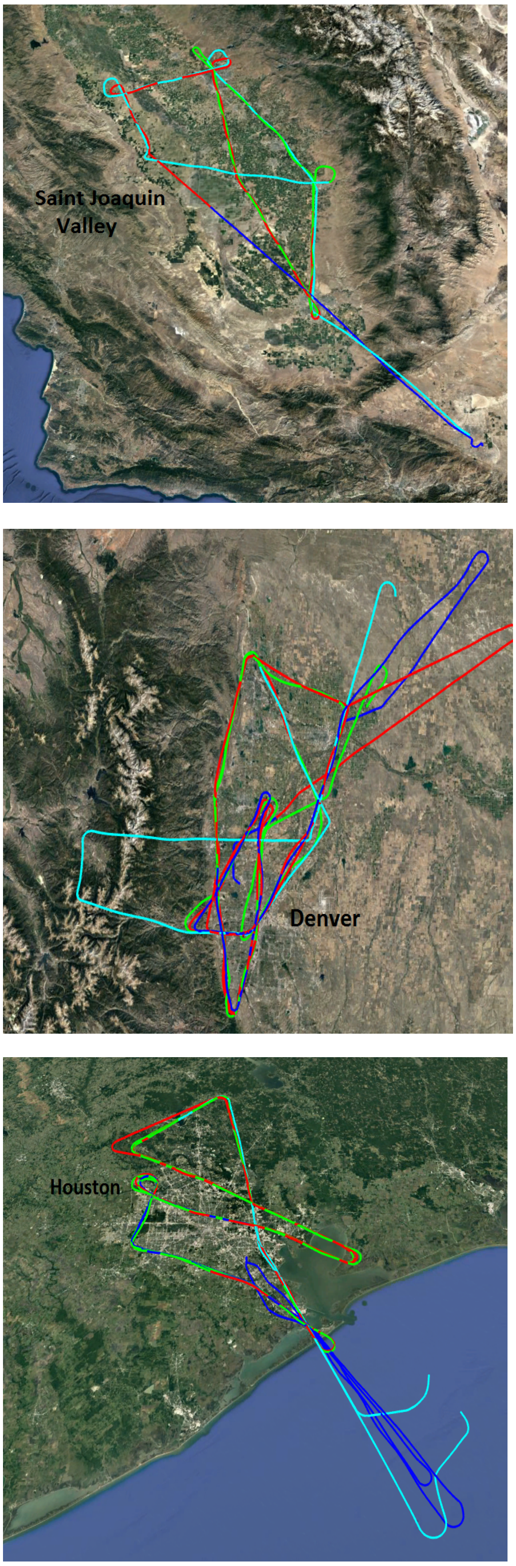

Figure 9: Flight tracks fof B200 NASA Airplane for the three different days used as examples during Discover-AQ(a) 30th January 2013 in California (b) 10th August 2014 in Colarado and (c) 26th September 2014 in Texas.

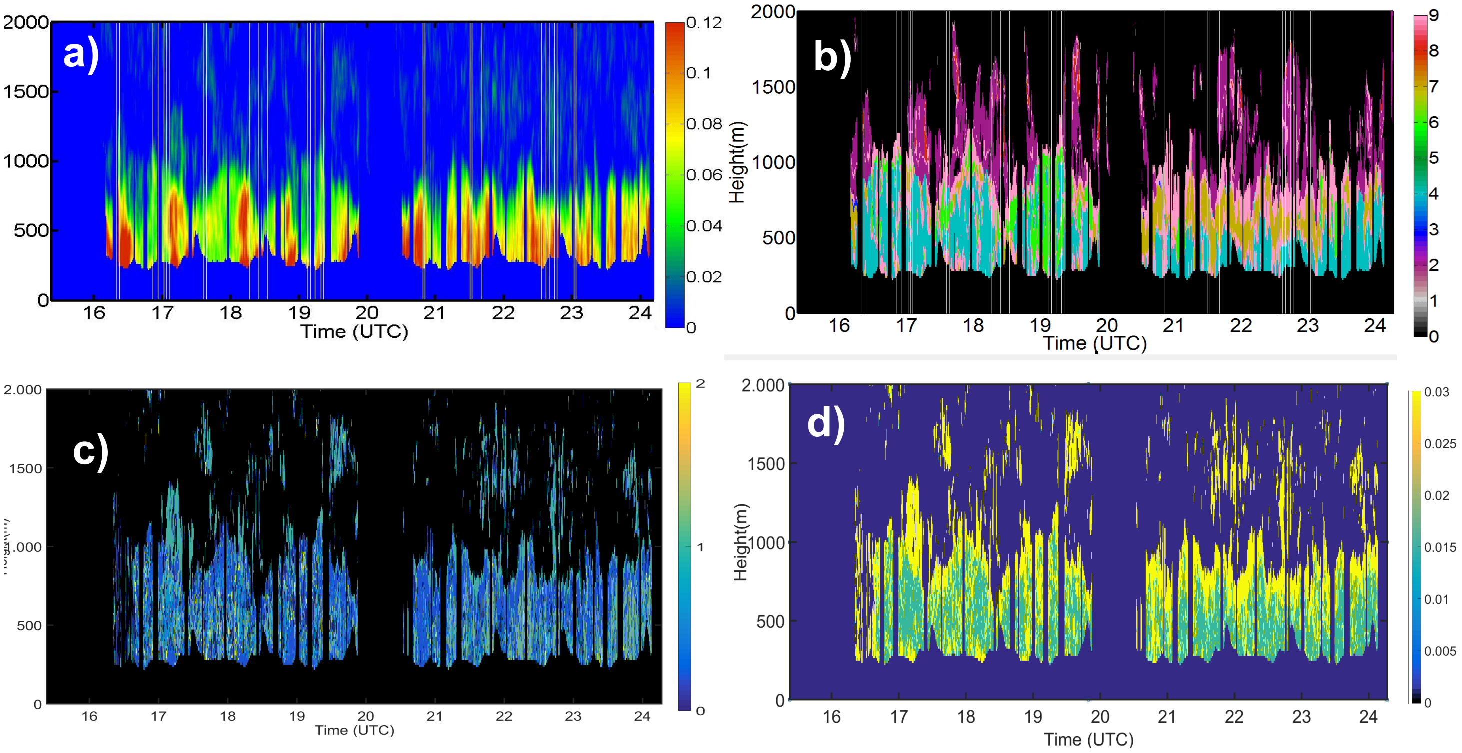

Figure 10: HSRL-2 airborne measurements during DISCOVER-AQ in California on 30th January 2013. (a)Extinction coefficient at 532 nm and (b) Aerosol typing ID where 0 is no classification attempted because data values are out of range, 1 = ice, 2 = dusty mix aerosol, 3 = maritime aerosol, 4 = urban/pollution aerosol, 5 = smoke, 6 = fresh smoke, 7 = polluted maritime aerosol, 8 = pure dust, 9 is unclassified due to the measured properties being consistent with more than one class. (c) Predominant type of particles from the algorithm for optimizing constraints, 1 = fine mode predominance and 2 = mixture of fine and coarse mode (d) estimated imaginary refractive index from the algorithm for optimizing constraints.

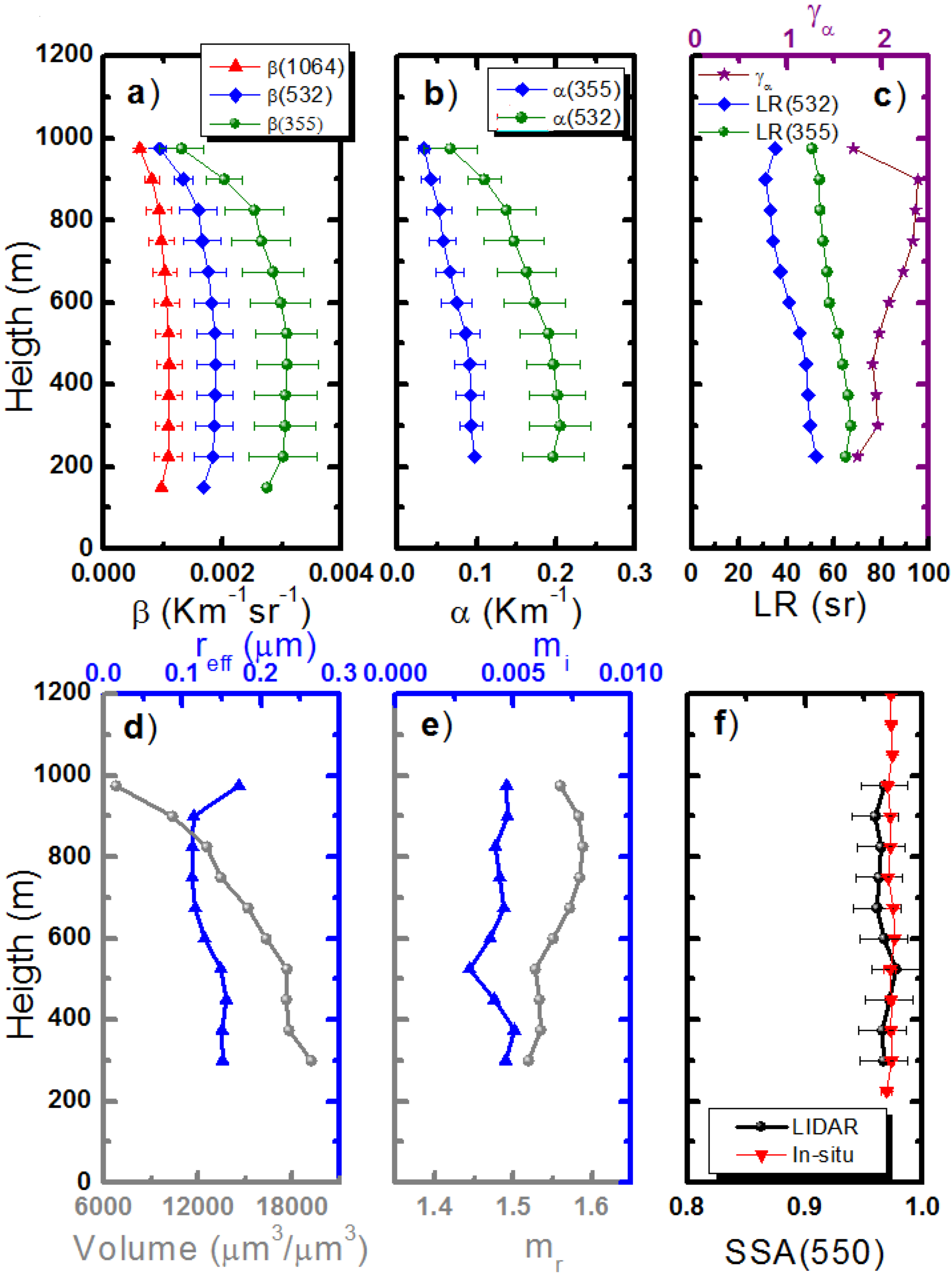

Figure 11: Vertical profiles of aerosol optical and microphysical properties form airborne HSRL-2 measurements on 30th January 2013 at 21:54 UTC. Correlative data of single scattering albedo (SSA) measured by in-situ instrumentation onboard P-3B airplane are also shown. Error bars are the uncertainties associated with each 3β+2α measurements while for SSA are the uncertainties associated with low absorption (±0.02).

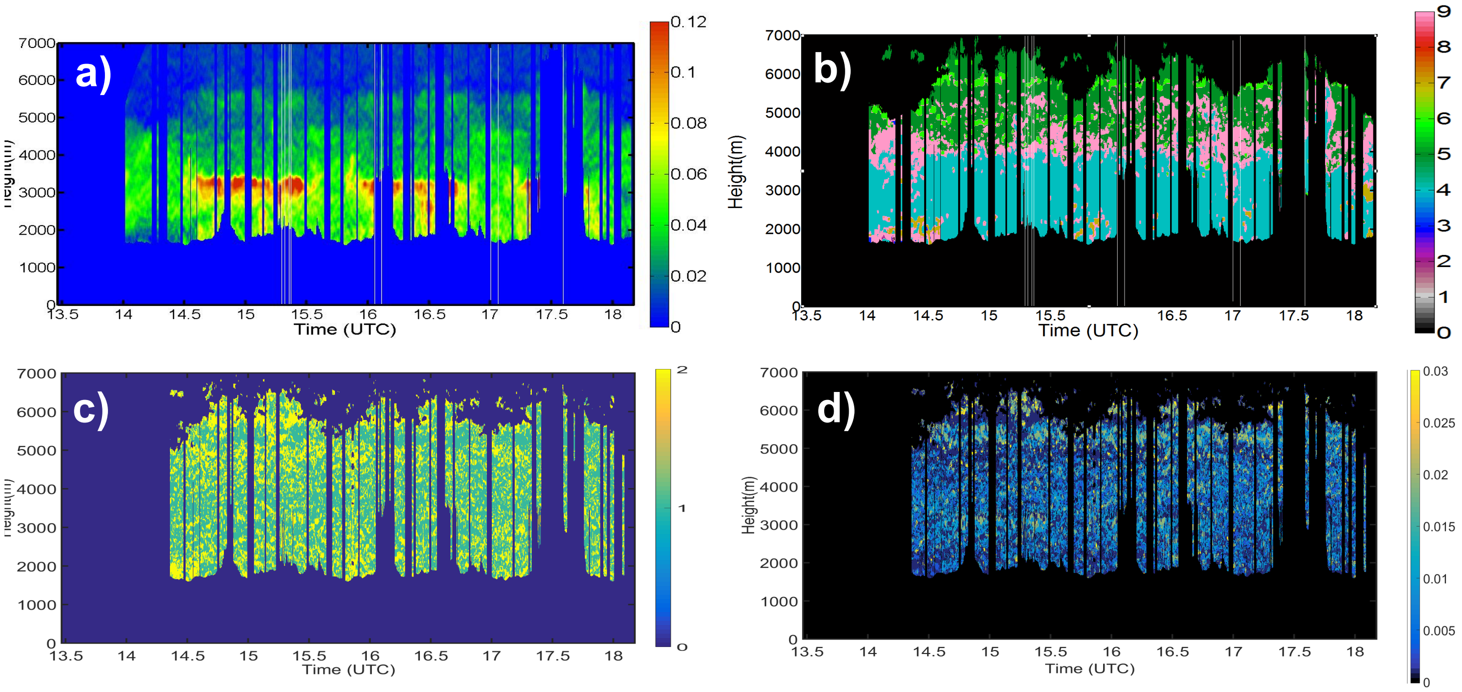

Figure 12: HSRL-2 airborne measurements during DISCOVER-AQ in Colorado on 10th August 2014. (a)Extinction coefficient at 532 nm and (b) Aerosol typing ID where 0 is no classification attempted because data values are out of range, 1 = ice, 2 = dusty mix aerosol, 3 = maritime aerosol, 4 = urban/pollution aerosol, 5 = smoke, 6 = fresh smoke, 7 = polluted maritime aerosol, 8 = pure dust, 9 is unclassified due to the measured properties being consistent with more than one class. (c) Predominant type of particles from the algorithm for optimizing constraints, 1 = fine mode predominance and 2 = mixture of fine and coarse mode (d) estimated imaginary refractive index from the algorithm for optimizing constraints.

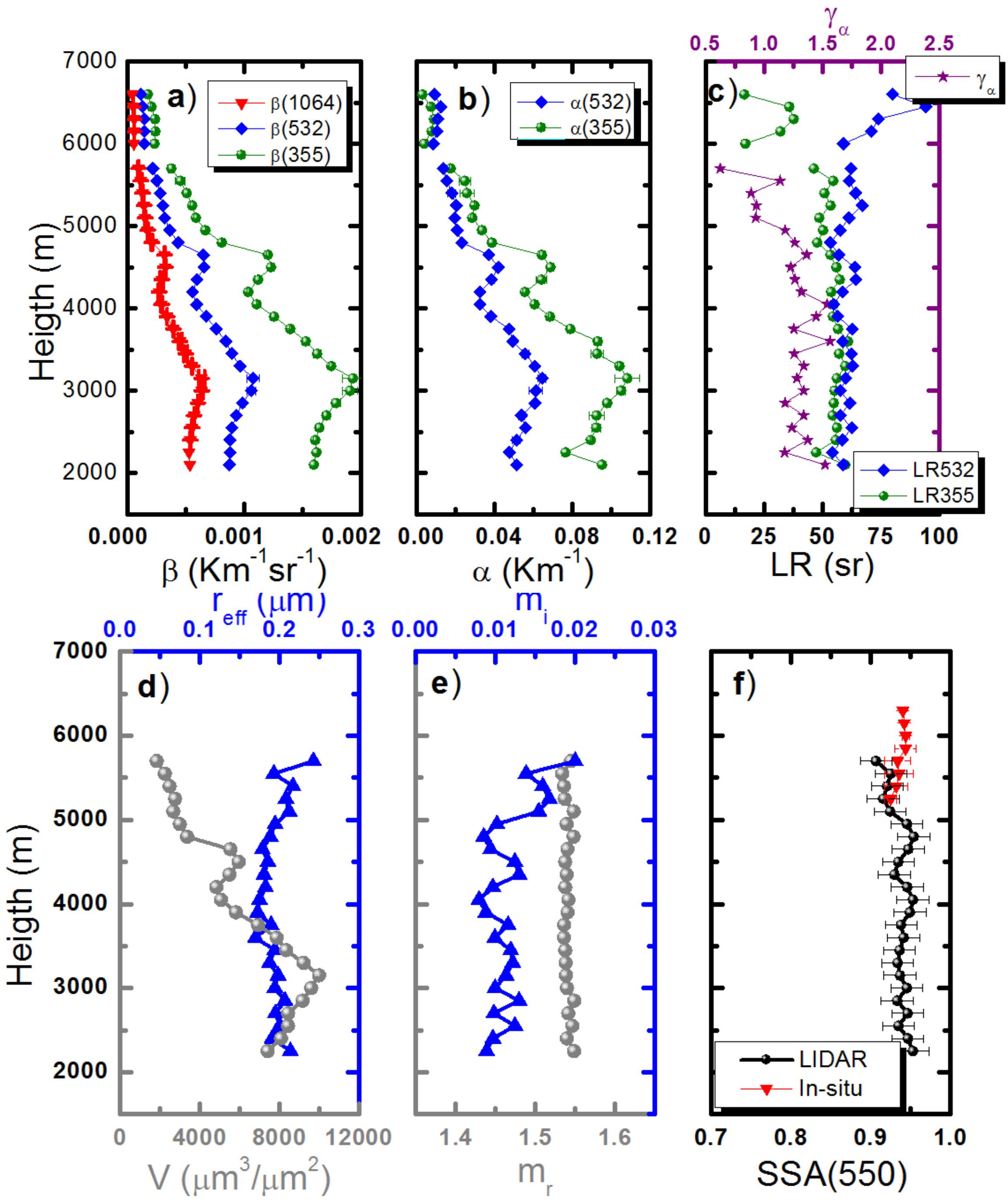

Figure 13: Vertical profiles of retrieved aerosol microphysical properties from airborne HSRL-2 measurements on 10th August 2014 at 15:30 UTC. Correlative data of single scattering albedo (SSA) measured by in-situ instrumentation onboard P-3B airplane are also shown. Error bars are the uncertainties associated with each 3β+2α measurements while for SSA are the uncertainties associated with medium absorption (±0.03).

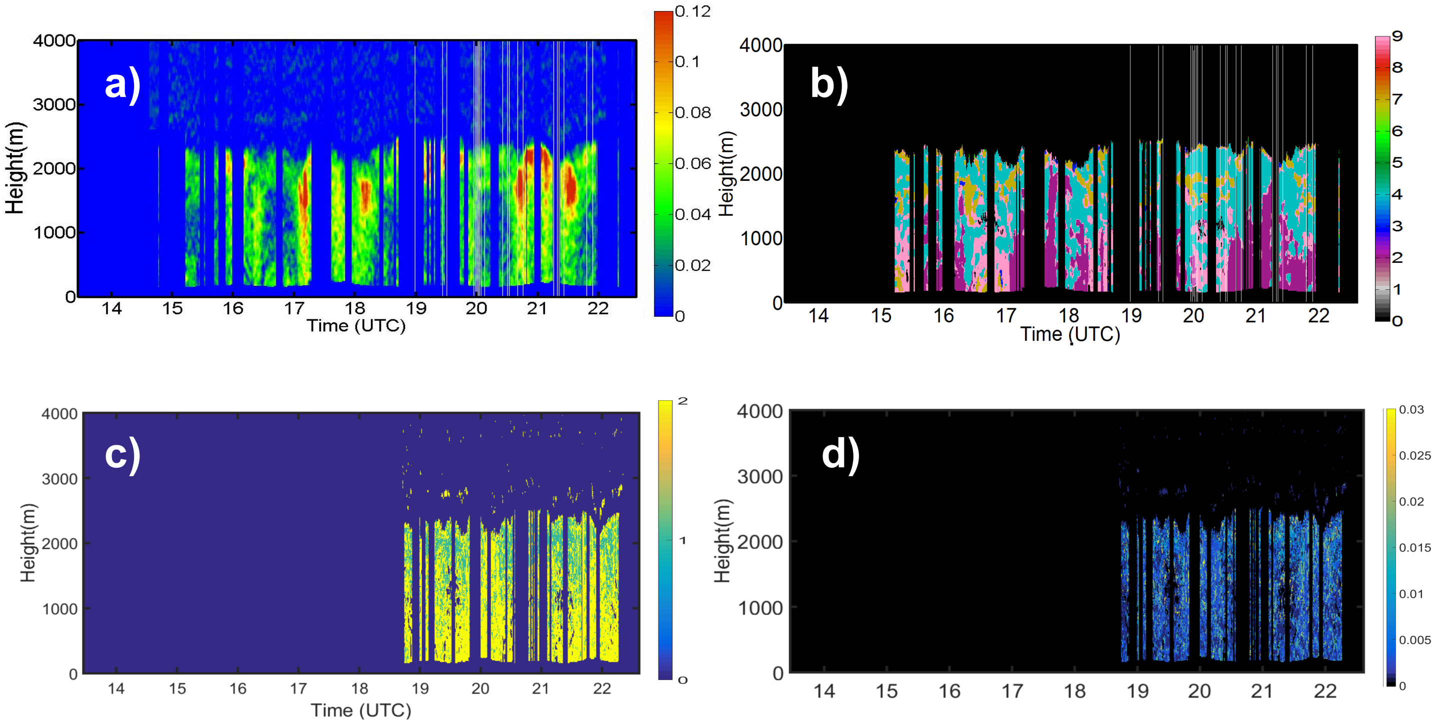

[**Figure 14:**]() HSRL-2 airborne measurements during DISCOVER-AQ n Houston area on 26th September 2013. (a)Extinction coefficient at 532 nm and (b) Aerosol typing ID where 0 is no classification attempted because data values are out of range, 1 = ice, 2 = dusty mix aerosol, 3 = maritime aerosol, 4 = urban/pollution aerosol, 5 = smoke, 6 = fresh smoke, 7 = polluted maritime aerosol, 8 = pure dust, 9 is unclassified due to the measured properties being consistent with more than one class. (c) Predominant type of particles from the algorithm for optimizing constraints, 1 = fine mode predominance and 2 = mixture of fine and coarse mode (d) estimated imaginary refractive index from the algorithm for optimizing constraints.

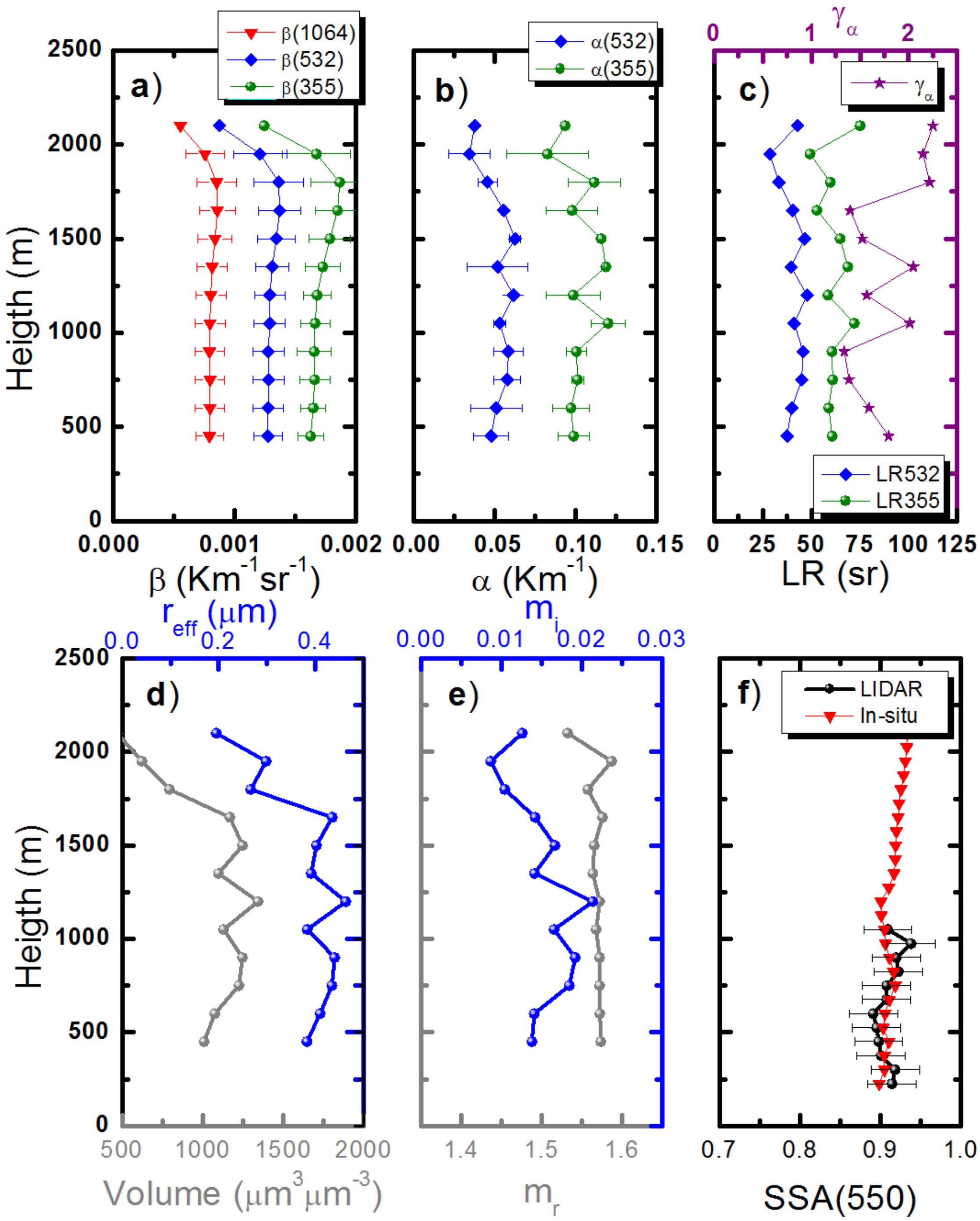

Figure 15: Vertical profiles of retrieved aerosol microphysical properties from airborne HSRL-2 measurements on 26th September 2013 at 20:40 UTC. Correlative data of single scattering albedo (SSA) measured by in-situ instrumentation onboard P-3B airplane are also shown. Error bars are the uncertainties associated with each 3β+2α measurements while for SSA are the uncertainties associated with medium absorption (±0.03).

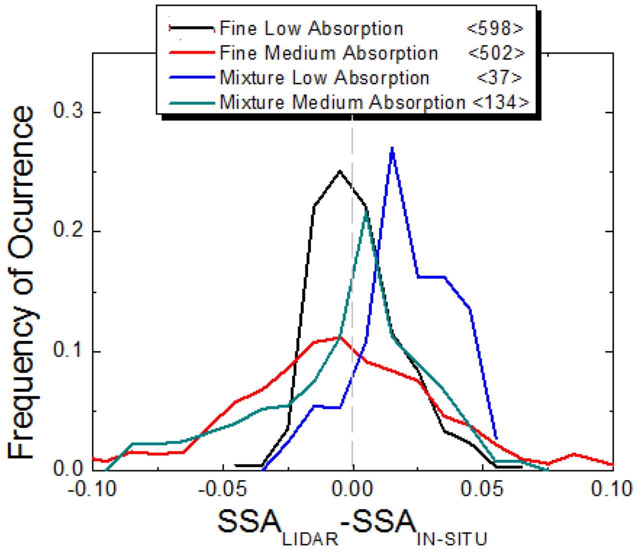

Figure 16: Frequency of occurrence of the differences in single scattering albedo (SSA) between the values retrieved by the stand-alone lidar inversion and these measured by in-situ measurements during DISCOVER-AQ field campaigns in California (2013), Texas (2014) and Colorado (2014). Results are plotted for fine mode predominance and mixture of mode cases, and also differentiating between low (mi < 0.01) and medium aerosol absorption (0.01 < mi < 0.04). The numbers of available measurements for intercomparsions for each case are given in within brackets.

			Retrieved m_r at 532 nm			Retrieved m_i at 532 nm			Retrieved SSA at 532 nm			Other aerosol parameters		
Site	**Type**	**N**	**Mean**	**Min.**	**Max.**	**Mean**	**Min.**	**Max.**	**Mean**	**Min.**	**Max.**	**AOD(440)**	**Alpha**	**r_{eff} (μm)**
Alta Floresta[a]	BB	673	1.47 ±0.05	1.35	1.60	0.010 ±0.005	0.001	0.045	0.92 ±0.03	0.80	0.99	1.15 ±0.64	1.88 ±0.17	0.21 ±0.04
Belterra[b]	BB	103	1.45 ±0.05	1.35	1.59	0.009 ±0.005	0.001	0.034	0.90 ±0.04	0.74	0.98	0.65 ±0.25	1.56 ±0.26	0.29 ±0.01
Bondville[b]	BB/P	450	1.41 ±0.05	1.33	1.48	0.006 ±0.004	0.001	0.025	0.96 ±0.03	0.97	1.00	0.62 ±0.22	1.77 ±0.20	0.21 ±0.04
Bratss Lake[b]	BB	112	1.48 ±0.04	1.37	1.55	0.006 ±0.002	0.001	0.018	0.94 ±0.02	0.89	1.00	0.60 ±0.17	1.81 ±0.22	0.23 ±0.05
Buenos Aires[a]	P	62	1.44 ±0.05	1.34	1.56	0.013 ±0.005	0.005	0.031	0.87 ±0.05	0.71	0.93	0.65 ±0.27	1.82 ±0.14	0.22 ±0.04
CART site[b]	BB	167	1.42 ±0.04	1.35	1.51	0.005 ±0.004	0.001	0.026	0.95 ±0.04	0.80	0.99	0.52 ±0.14	1.74 ±0.15	0.26 ±0.04
Chiang Mai[e]	BB/P	1987	1.46 ±0.05	1.35	1.60	0.020 ±0.009	0.003	0.057	0.92 ±0.03	0.80	0.99	0.93 ±0.49	1.61 ±0.16	0.23 ±0.05
Cuiaba[a]	BB	555	1.48 ±0.04	1.37	1.60	0.016 ±0.005	0.001	0.049	0.86 ±0.05	0.70	0.99	0.95 ±0.51	1.78 ±0.13	0.23 ±0.04
GSFC[b]	P	1107	1.42 ±0.04	1.33	1.58	0.005 ±0.003	0.001	0.048	0.95 ±0.02	0.73	1.00	0.66 ±0.25	1.82 ±0.20	0.23 ±0.04
Hong Kong[e]	P/BB	178	1.44 ±0.03	1.34	1.51	0.014 ±0.009	0.004	0.070	0.89 ±0.04	0.72	0.97	0.82 ±0.35	1.41 ±0.15	0.27 ±0.04
Ilorin[d]	BB	53	1.49 ±0.06	1.35	1.60	0.018 ±0.009	0.001	0.043	0.82 ±0.06	0.72	0.98	0.72 ±0.23	1.29 ±0.30	0.33 ±0.14
Ispra[d]	P	505	1.41 ±0.05	1.33	1.58	0.010 ±0.006	0.001	0.039	0.92 ±0.04	0.75	0.99	0.67 ±0.26	1.54 ±0.23	0.27 ±0.07
Ji Parana[a]	BB	491	1.48 ±0.05	1.34	1.60	0.011 ±0.004	0.001	0.027	0.92 ±0.02	0.84	0.99	1.15 ±0.64	1.12 ±0.60	0.20 ±0.03
Mbita[c]	BB	101	1.44 ±0.06	1.35	1.59	0.011 ±0.005	0.002	0.029	0.88 ±0.04	0.74	0.97	0.55 ±0.14	1.54 ±0.20	0.32 ±0.11
Mexico City[b]	P/BB	491	1.42 ±0.06	1.33	1.60	0.013 ±0.006	0.001	0.042	0.89 ±0.04	0.76	0.99	0.64 ±0.21	1.68 ±0.15	0.26 ±0.05
Mongu[c]	BB	1893	1.50 ±0.05	1.34	1.60	0.024 ±0.008	0.001	0.058	0.85 ±0.03	0.71	0.99	0.67 ±0.25	1.88 ±0.11	0.20 ±0.03
Moscow[d]	P/BB	305	1.45 ±0.06	1.33	1.60	0.013 ±0.009	0.007	0.053	0.90 ±0.05	0.73	0.99	0.74 ±0.48	1.69 ±0.14	0.24 ±0.04
Mukdahan[e]	BB	1022	1.45 ±0.04	1.35	1.60	0.013 ±0.006	0.001	0.056	0.90 ±0.04	0.78	1.00	0.78 ±0.30	1.55 ±0.16	0.25 ±0.05
Paris[d]	P	113	1.39 ±0.04	1.33	1.51	0.008 ±0.004	0.001	0.022	0.94 ±0.03	0.78	0.99	0.56 ±0.13	1.58 ±0.19	0.23 ±0.04
Pimai	BB/P	598	1.43 ±0.05	1.34	1.60	0.013 ±0.005	0.001	0.030	0.90 ±0.03	0.81	1.00	0.77 ±0.30	1.52 ±0.16	0.28 ±0.08
Rio Branco[a]	BB	422	1.47 ±0.04	1.36	1.59	0.015 ±0.006	0.001	0.043	0.90 ±0.03	0.79	1.00	0.91 ±0.50	1.87 ±0.12	0.21 ±0.03
Santa Cruz[a]	BB/P	174	1.48 ±0.04	1.36	1.59	0.013 ±0.008	0.003	0.067	0.90 ±0.05	0.69	0.97	1.10±0.57	1.78 ±0.12	0.22 ±0.04
Shouxian[e]	P/BB	223	1.46 ±0.06	1.34	1.60	0.012 ±0.006	0.001	0.042	0.90 ±0.04	0.77	0.99	0.85 ±0.34	1.21 ±0.25	0.33 ±0.13
Silpakorn[e]	BB/P	1750	1.46 ±0.04	1.35	1.60	0.015 ±0.006	0.001	0.042	0.88 ±0.04	0.73	0.88	0.76 ±0.27	1.52 ±0.17	0.27 ±0.06
Singapore[e]	BB/P	184	1.41 ±0.04	1.34	1.59	0.007 ±0.003	0.001	0.021	0.95 ±0.03	0.85	1.00	0.71 ±0.36	1.50 ±0.22	0.27 ±0.09
Taihu[e]	P/BB	621	1.42±0.05	1.34	1.55	0.012 ±0.006	0.001	0.048	0.90 ±0.04	0.75	0.99	0.93 ±0.40	1.42 ±0.17	0.27 ±0.05
Ubon Ratchathni[e]	BB/P	787	1.45 ±0.04	1.35	1.58	0.011 ±0.005	0.001	0.035	0.91 ±0.03	0.80	0.91	0.94 ±0.37	1.63 ±0.13	0.23 ±0.04
Yakutsk[c]	BB/P	98	1.48 ±0.05	1.36	1.59	0.007 ±0.006	0.001	0.036	0.95 ±0.03	0.82	0.96	0.81±0.44	1.84 ±0.25	0.20 ±0.06
Zambezi[d]	BB	220	1.49 ±0.05	1.36	1.59	0.024 ±0.006	0.006	0.041	0.85 ±0.03	0.78	0.93	0.87 ±0.36	1.89 ±0.14	0.18 ±0.03

Table 1: Mean values, standard deviations, maximum and minimum values of retrieved real refractive index (m_i), imaginary refractive index (m_r) and single scattering albedo (SSA) from AERONET Level 2.0 almucantar inversions. Reference wavelength is 532 nm and data are computed for linear interpolations of retrieved values at 440 and 670 nm. For data that fullfill conditions for single scattering albedo conditions, mean and standard deviations of aerosol optical depth (AOD), Angstrom parameter (α(440-870)) and effective radius (r_{eff}) are also given. Retrievals are limited to those with sphericity parameter larger than 70% consistent with the use of Mie functions in the inversion. The sites selected are affected by biomass burning (BB) and/or pollution (P) aerosol. The sites are representative of different locations: a) South America, b) North America, d) Africa, d) Europe, e) Asia.

		r_{eff} (µm)	σ (µm)	$m_{r,355}$	$m_{r,532}$	$m_{r,1064}$	$m_{i,355}$	$m_{i,532}$	$m_{i,1064}$
Sulphate	**Dry** **Humid**	0.157 0.257	2.03	1.45 1.37	1.43 1.36	1.42 1.35	1E-8 7E-9	1E-8 4E-9	3E-6 8E-6
Organic Carbon	**Dry** **Humid**	0.088 0.126	2.20	1.53 1.41	1.53 1.40	1.52 1.39	0.0050 0.0017	0.0056 0.0019	0.0164 0.0055
Black Carbon	**Dry** **Humid**	0.039 0.047	2.00	1.75 1.58	1.75 1.58	1.76 1.58	0.4645 0.2756	0.4436 0.2632	0.4426 0.2626
Sea Salt	**Dry** **Humid**	0.078 0.126	2.03	1.51 1.39	1.50 1.38	1.47 1.36	3E-7 8E-8	1E-8 4E-9	2E-4 6E-5
	Dry **Humid**	0.266 0.438	2.03	1.51 1.38	1.50 1.37	1.47 1.36	3E-7 8E-8	1E-8 4E-9	2E-4 5E-5
	Dry **Humid**	1.072 1.818	2.03	1.51 1.38	1.50 1.37	1.47 1.36	3E-7 7E-8	1E-8 4E-9	2E-4 5E-5
	Dry **Humid**	2.551 4.388	2.03	1.51 1.38	1.50 1.37	1.47 1.36	3E-7 6E-8	1E-8 4E-9	2E-4 5E-5
	Dry **Humid**	7.339 12.96	2.03	1.51 1.37	1.50 1.36	1.47 1.35	3E-7 6E-8	1E-8 4E-9	2E-4 4E-5

Table 2: Size distribution and refractive index properties of the different aerosol species included in GOCART that can be assumed as spherical particles. All species are assumed hygroscopic and we present values at dry (RH = 0 %) and humid conditions (80%). The width of the distribution is assumed to not vary as a function of relative humidity.

	m_i	$r_f = 0.075$ µm		$r_f = 0.10$ µm		$r_f = 0.14$ µm		$r_f = 0.18$ µm	
		LR_{355}	LR_{532}	LR_{355}	LR_{532}	LR_{355}	LR_{532}	LR_{355}	LR_{532}
$m_r = 1.35$	0	54.0	27.0	77.9	44.4	94.5	72.8	100.6	88.6
	0.001	54.8	27.6	79.1	45.1	96.4	73.9	103.1	90.3
	0.005	57.9	29.8	84.2	47.8	104.5	78.4	113.6	96.9
	0.01	61.9	32.6	90.8	51.2	115.1	84.2	127.7	105.6
	0.025	74.1	40.9	11.3	61.5	150.1	102.3	176.0	133.7
	0.05	94.8	54.9	147.3	78.9	216.7	133.7	273.8	184.9
	0.075	114.8	68.5	183.0	95.7	287.0	164.5	381.6	237.4
	0.1	133.2	81.0	215.9	11.22	353.3	192.8	482.5	286.5
$m_r = 1.45$	0	53.1	28.2	68.5	45.0	68.5	66.0	59.0	70.9
	0.001	53.7	28.6	69.6	45.5	70.1	67.0	60.7	72.2
	0.005	56.2	30.1	73.9	47.5	76.5	70.8	67.9	77.9
	0.01	59.4	31.9	79.5	50.0	85.1	75.7	77.8	85.2
	0.025	68.9	37.5	97.2	57.6	114.5	91.1	113.4	109.4
	0.05	84.9	46.8	128.2	70.4	173.0	117.6	194.1	154.7
	0.075	100.3	55.9	159.0	82.7	238.0	143.6	294.1	202.1
	0.1	114.5	64.7	187.4	94.2	300.8	167.4	395.2	246.8
$m_r = 1.55$	0	52.7	29.8	59.0	46.1	44.3	59.3	29.0	53.0
	0.001	53.3	30.1	60.0	46.5	45.4	60.2	29.9	54.2
	0.005	55.6	31.2	64.2	48.3	50.2	64.0	33.9	59.0
	0.01	58.6	32.6	69.5	50.5	56.7	68.7	39.3	65.4
	0.025	67.5	36.9	86.7	57.3	79.7	83.8	60.1	86.9
	0.05	82.2	43.9	117.7	68.2	130.4	110.2	112.8	130.3
	0.075	96.0	50.8	149.0	78.6	193.8	136.0	190.8	179.1
	0.1	108.4	57.4	177.7	88.1	261.0	159.4	286.6	226.9
$m_r = 1.65$	0	50.9	31.7	46.8	46.7	26.9	49.6	15.3	36.1
	0.001	51.5	32.0	47.7	47.1	27.6	50.5	15.8	37.0
	0.005	53.9	32.9	51.3	48.9	30.6	54.0	17.8	40.5
	0.01	56.9	34.1	56.0	51.2	34.6	58.5	20.7	45.1
	0.025	66.1	37.7	71.8	57.9	49.3	73.1	31.4	61.5
	0.05	81.3	43.6	102.1	68.6	83.7	99.9	58.8	97.0
	0.075	95.3	49.2	135.0	78.4	131.8	127.6	102.1	141.5
	0.1	107.6	54.5	166.7	87.1	190.7	153.3	162.6	190.5

Table 3: Extinction-to-backscattering ratio (LR) at 355 and 532 nm for bimodal size distribution with different sets of refractive indexes $m = m_r + im_i$ and different sets of modal radiuses r_M of 0.075, 0.10, 0.14 and 0.18 µm (fine mode predominance size distribution). The width of the mode is fixed to σ_M =0.4 µm

	m_r	r_f = 0.075 µm		r_f = 0.10 µm		r_f = 0.14 µm		r_f = 0.18 µm	
		$\gamma_{\alpha(355-532)}$	$\frac{LR_{355}}{LR_{532}}$	$\gamma_{\alpha(355-532)}$	$\frac{LR_{355}}{LR_{532}}$	$\gamma_{\alpha(355-532)}$	$\frac{LR_{355}}{LR_{532}}$	$\gamma_{\alpha(355-532)}$	$\frac{LR_{355}}{LR_{532}}$
m_i = 0.005	1.35	2.59	1.95	2.29	1.76	1.86	1.33	1.48	1.17
	1.45	2.58	1.87	2.18	1.56	1.61	1.08	1.14	0.87
	1.55	2.53	1.78	2.03	1.33	1.34	0.79	0.80	0.57
	1.65	2.45	1.64	1.84	1.05	1.07	0.57	0.49	0.44
m_i = 0.025	1.35	2.24	1.81	2.04	1.81	1.69	1.47	1.35	1.31
	1.45	2.34	1.84	2.01	1.69	1.50	1.26	1.06	1.04
	1.55	2.35	1.83	1.90	1.51	1.27	0.95	0.76	0.69
	1.65	2.31	1.75	1.75	1.24	1.02	0.67	0.47	0.51
m_i = 0.05	1.35	1.95	1.72	1.81	1.87	1.51	1.62	1.21	1.48
	1.45	2.01	1.81	1.83	1.82	1.37	1.47	0.97	1.26
	1.55	2.16	1.87	1.76	1.72	1.18	1.18	0.70	0.87
	1.65	2.16	1.86	1.65	1.49	0.96	0.84	0.44	0.60
m_i = 0.075	1.35	1.75	1.68	1.63	1.91	1.35	1.75	1.09	1.61
	1.45	1.92	1.79	1.67	1.92	1.26	1.66	0.89	1.46
	1.55	2.00	1.89	1.64	1.90	1.10	1.42	0.66	1.07
	1.65	2.02	1.94	1.55	1.72	0.90	1.03	0.42	0.72

Table 4: Angstrom exponent of extinction (γ_α) and ratio between extinction-to-backscattering ratio (LR) at 355 and 532 nm for unimodal size distribution with different sets of refractive indexes m = m_r + im_i and different sets of modal radiuses r_M of 0.075, 0.10, 0.14 and 0.18 µm (fine mode predominance size distribution). The width of the mode is fixed to σ_M =0.4 µm.

	V_f/V_c = 2		V_f/V_c = 1		V_f/V_c = 0.5		V_f/V_c = 0.2		V_f/V_c = 0.1	
m_i	**LR355**	**LR532**	**LR355**	**LR532**	**LR355**	**LR532**	**LR355**	**LR532**	**LR355**	**LR532**
0	32.4	29.0	26.5	21.1	20.6	15.8	14.6	11.0	11.9	9.3
0.005	41.8	37.4	36.6	28.6	30.6	21.6	23.6	16.0	20.1	13.7
0.01	49.8	44.8	45.2	35.7	39.5	27.9	32.1	21.1	28.1	18.3
0.025	76.1	67.8	73.3	59.3	69.4	50.7	63.3	41.7	59.2	37.5
0.05	131.9	106.6	133.1	104.1	135.2	100.9	139.0	96.4	142.0	93.8

Table 5: Extinction-to-backscattering ratio (LR) at 355 and 532 nm for bimodal size distribution with fine mode at r_{fine} = 0.14 µm and σ_{fine} = 0.4 µm and coarse mode with r_{coarse}= 1.5 µm and σ_{coarse} = 0.6 µm. The real part of refractive index (m_r) is fixed to 1.55 while imaginary part (m_i) is variable.